Title: Microtubule networks in zebrafish hair cells facilitate presynapse transport and fusion during development

Saman Hussain[1], Katherine Pinter[1], Mara Uhl[2,3], Hiu-Tung Wong[1], and Katie Kindt[1]

[1]Section on Sensory Cell Development and Function, National Institute on Deafness and other Communication Disorders, Bethesda, MD, 20892, USA

[2]Presynaptogenesis and Intracellular Transport in Hair Cells Junior Research Group, Institute for Auditory Neuroscience and InnerEarLab, University Medical Center Goettingen, 37075 Goettingen, Germany

[3]Collaborative Research Center 889 '*Cellular Mechanisms of Sensory Processing*', 37075 Goettingen, Germany

Correspondence: katie.kindt@nih.gov

Abstract (160)

Sensory cells in the retina and inner ear rely on specialized ribbon synapses for neurotransmission. Disruption of these synapses is linked to visual and auditory dysfunction, but it is unclear how these unique synapses are formed. Ribbon synapses are defined by a presynaptic density called a ribbon. Using live-imaging approaches in zebrafish, we find that early in hair-cell development, many small ribbon precursors are present throughout the cell. Later in development, fewer and larger ribbons remain, and localize at the presynaptic active zone (AZ). Using tracking analyses, we show that ribbon precursors exhibit directed motion along an organized microtubule network towards the presynaptic AZ. In addition, we show that ribbon precursors can fuse together on microtubules to form larger ribbons. Using pharmacology, we find that microtubule disruption interferes with ribbon motion, fusion, and normal synapse formation. Overall, this work demonstrates a dynamic series of events that underlies formation of a critical synapse required for sensory function.

Introduction

The inner ear and retina contain sensory cells that rely on specialized ribbon synapses that faithfully transmit the timing, duration, and intensity of sensory stimuli to the brain. Ribbon synapses are critical for human hearing and vision–disruption of these synapses is linked to auditory and visual disorders (Frederick and Zenisek, 2023; Kujawa and Liberman, 2015). The hallmark feature of these synapses is a presynaptic specialization called a ribbon, which is a dense body made up primarily of the protein Ribeye (Schmitz et al., 2000). Ribbons are found at the presynaptic active zone (AZ) and act as a scaffolds to ready synaptic vesicles for release (Schmitz, 2009). During development, small ribbon precursors are hypothesized to migrate to the presynaptic AZ and fuse to form larger, mature ribbons. However, there is no direct evidence for precursor migration or fusion, and the dynamic processes underlying ribbon formation remain unclear.

Neurotransmission at mature ribbon synapses is triggered in response to graded membrane depolarizations dictated by the duration and intensity of sensory stimuli. Membrane depolarization opens voltage-gated calcium channels (Ca_V1) beneath ribbons (Brandt et al., 2003; Chang et al., 2006) (see schematic in Figure 1C). Calcium influx triggers the fusion of synaptic vesicles secured near the ribbon, resulting in release of the glutamate onto postsynaptic receptors (Obholzer et al., 2008; Ruel et al., 2008). Studies in mouse and zebrafish have shown that Ribeye, along with $Ca_V1.4$ (photoreceptors) and $Ca_V1.3$ (hair cells) channels play important, interconnected roles in the formation of ribbon synapses (Jia et al., 2014; Mansergh et al., 2005; Nemzou N. et al., 2006; Sheets et al., 2012). For example, in mice and zebrafish lacking functional Ca_V1 channels, ribbon formation is disrupted, and fewer complete synapse are formed. Similarly, when Ribeye is knocked out in mouse or zebrafish, Ca_V1 channel localization is disrupted at ribbon synapses of photoreceptors and hair cells (Jean et al., 2018; Maxeiner et al., 2016; Sheets et al., 2011). In addition to Ribeye, the classic neuronal scaffolding proteins Bassoon and a novel variant of Piccolo, Piccolino have been shown to be important components of ribbon synapses (Gundelfinger et al., 2016). In mice, work has shown that in sensory cells lacking Bassoon ribbons are not properly anchored at the presynaptic AZ, and synapse function is disrupted (Dick et al., 2003; Frank et al., 2010; Khimich et al., 2005). In rats,

60 loss of Piccolino also impacts ribbon morphology (Michanski et al., 2023; Regus-Leidig et al.,
61 2014). Currently how these key molecular players fit within the dynamics underlying ribbon
62 formation is not completely understood.

63 In neurons, precursor vesicles containing Piccolo and Bassoon have been shown to be
64 transported along a network of microtubule tracks to the developing presynaptic AZ. (Ahmari et
65 al., 2000; Gundelfinger et al., 2016; Maas et al., 2012; Shapira et al., 2003). Transport requires
66 molecular motors, along with adaptor proteins, to move cargos along microtubules in a
67 directional manner (Bury and Sabo, 2011; Fejtova et al., 2009; Maas et al., 2012). In neurons,
68 kinesins are the molecular motors that transport cargos in the anterograde direction–away
69 from the cell body and towards the presynaptic AZ, and cytoplasmic dynein is the motor that
70 moves cargos in a retrograde manner (Sweeney and Holzbaur, 2018). Although it is currently
71 unclear what kinesin transports Piccolo-Bassoon transport vesicles, recent work in *Drosophila*
72 and *C. elegans* suggests that the kinesin KIF1A may transport AZ components (Oliver et al.,
73 2022; Pack-Chung et al., 2007). Work in developing photoreceptors, has shown that ribbon
74 precursors contain not only Ribeye, but also Bassoon, and the ribbon synapse specific isoform
75 of Piccolo, Piccolino (Regus-Leidig et al., 2009). Further, work in developing mouse auditory
76 inner hair cells (IHCs) has shown that ribbon precursors contain both Piccolino and Ribeye
77 (Michanski et al., 2019). Whether these precursors are actively transported along microtubules
78 during ribbon-synapse formation as in neurons is not known.

79 Ribbon-synapse formation has been well studied using light and electron microscopy in
80 fixed tissues (Michanski et al., 2019; Regus-Leidig et al., 2009; Schmitz, 2009; Sheets et al.,
81 2011; Sobkowicz et al., 1986, 1982). Studies in mouse auditory inner hair cells (IHCs) have
82 shown that the majority of ribbon-synapse formation spans a large time window: E18-P14
83 (Michanski et al., 2019; Sobkowicz et al., 1986, 1982). In contrast to mice, ribbon synapses form
84 along a condensed timeline in zebrafish hair cells: 12-18 hrs (Dow et al., 2015; Sheets et al.,
85 2011). In both mouse IHCs and zebrafish hair cells, at the earliest stages of development there
86 are many small ribbon precursors throughout the cell–these precursors are thought to form via
87 self-aggregation of Ribeye within the cytosol (Magupalli et al., 2008; Schmitz et al., 2000). As
88 development progresses ribbons become larger, localize to the presynaptic AZ and associate

89 with the innervating afferent processes. Finally, the number of ribbons associated with
90 postsynaptic machinery is refined to obtain the proper number of complete synapses. Recent
91 work in mice has shown that ribbon precursors associate with microtubules (Michanski et al.,
92 2019), and it has been proposed that ribbon precursors migrate along tracks of microtubules to
93 reach the presynaptic AZ and during synapse refinement. Currently the *in vivo* dynamics of
94 ribbon precursors and microtubules during these developmental events are not known.

95 To understand how ribbons form, we have studied hair cells and developing ribbons in
96 the zebrafish lateral line (Figure 1A). The lateral line is a sensory system that allows aquatic
97 vertebrates to sense local water movements (Freeman, 1928; Suli et al., 2012). This sensory
98 system is composed of clusters of hair cells called neuromasts that are arranged in lines along
99 the surface of the fish. The posterior lateral line (pLL) forms an array of neuromasts along the
100 zebrafish trunk; in the pLL hair cells begin to form when larvae are 2 days post fertilization (dpf)
101 (see Figure 1A-B, D). By 5 dpf, the majority of hair cells are mature, and the lateral-line system
102 is functional (Suli et al., 2012). At these early ages zebrafish are transparent, and hair cells in
103 the lateral line can easily be studied *in vivo* for durations encompassing large portions of ribbon
104 formation (Dow et al., 2015). Further, transgenic lines expressing fluorescently tagged proteins
105 allow the visualization of subcellular dynamics, such as ribbon formation, in living zebrafish, at
106 high resolution.

107 During our study, we have worked in close collaboration with another group focused on
108 later aspects of ribbon formation and refinement in mouse auditory IHCs (at postnatal stages).
109 This work is published in a companion paper (Vorn et al.). Together our studies demonstrate
110 that ribbon transport along microtubules networks is important to properly form ribbons during
111 hair-cell development in mouse and zebrafish. Our *in vivo* zebrafish work leverages transgenic
112 lines that label: developing ribbons, microtubule networks, and the growing plus-ends of
113 microtubules. We use these lines, along with high-resolution imaging to visualize the dynamics
114 of ribbon formation. Using live imaging, we show that at the earliest stages of synapse
115 development, many small ribbon precursors are present throughout the cell. At later stages
116 fewer, larger ribbons remain, and localize to the base of the cell. We find that microtubule
117 networks in lateral-line hair cells are highly dynamic and grow plus-ends towards the

118 presynaptic AZ (the direction taken by most kinesin motors) (Sweeney and Holzbaur, 2018).
119 Using tracking analyses, we show that during development, ribbon precursors show directed
120 motion towards the presynaptic AZ. Further, we show that ribbon precursors move along and
121 can fuse together on microtubules. Lastly, we find that an unperturbed microtubule network is
122 critical for ribbon motion, fusion, and normal ribbon-synapse formation. Overall, this
123 foundational knowledge of ribbon formation provides fundamental insight on processes
124 needed to reform ribbon synapses that are lost, such as after noise-induced and age-related
125 hearing loss.
126
127 **Results**
128 **Time-course of ribbon formation in living zebrafish lateral-line hair cells**
129 Fixed preparations in zebrafish and mice have outlined a conserved process that underlies
130 ribbon or presynapse development in hair cells (Michanski et al., 2019; Sheets et al., 2011). At
131 the earliest stages of development, small ribbon precursors are found free-floating throughout
132 the cytoplasm. When mature, ribbons are found predominantly at presynaptic AZs, opposing
133 postsynaptic densities. To examine the dynamics underlying ribbon formation in more detail,
134 we studied hair cells in the zebrafish pLL. These hair cells form 3-4 ribbon synapses in just 12-18
135 hrs (Dow et al., 2015; Kindt et al., 2012). To image hair cells, ribbon precursors and ribbons *in*
136 *vivo* we used a double transgenic line. One transgenic line labels microtubules and serves as a
137 hair-cell marker (*myo6b:YFP-tubulin*). The other transgenic line labels ribbons and smaller
138 ribbon precursors (*myo6b:riba-TagRFP*) in hair cells (example, Figure 1D).
139 For our initial analyses, we assessed the overall time course of ribbon formation in hair
140 cells in the posterior lateral-line (pLL) when larvae were 2 dpf (Figure 1A). At 2 dpf each
141 neuromast contains 4-8 developing hair cells at different developmental stages (Figure 1B,D,F-
142 H). We used the height of the kinocilium (see schematic in Figure 1B), the tallest part of the
143 apical hair bundle (mechanosensory structure), to estimate the developmental stage of hair
144 cells as described previously (Stage: hair bundle height; early: <1.5 µm, intermediate: 1.5-
145 10 µm, late: 10-18 µm, mature: >18 µm (Zhang and Kindt, 2022)). Qualitatively, we observed
146 that at early and intermediate stages, small Riba-TagRFP puncta were present throughout the

147 cell body (examples, Figure 1D,F-G). By late stages, or in newly matured hair cells, larger Riba-
148 TagRFP puncta were restricted to the base of the cell (example, Figure 1H). We quantified the
149 total number of Riba-TagRFP puncta based on developmental stage and found that the total
150 number of puncta was high at early and intermediate stages, but significantly decreased when
151 hair cells were mature (Figure 1E, Figure 1-S1A, n = 7 neuromasts and 67 hair cells).
152 When taking these live images, we had no postsynaptic marker and were unable to
153 differentiate between precursors and smaller ribbons associated with a postsynaptic density.
154 Therefore, we classified all apical Riba-TagRFP puncta above the nucleus as precursors, and all
155 ribbons located beneath the nucleus at the cell base were classified as more mature ribbons.
156 Using this classification, we quantified the total number of Riba-TagRFP puncta at each
157 developmental stage (Figure E, Figure 1-S1B-C, n = 7 neuromasts and 67 hair cells). We found
158 that apical Riba-TagRFP precursors were only present at early and intermediate stages (Figure
159 1E, Figure 1-S1B, and see yellow arrows in Figure 1F-G). In contrast, hair cells at late stages or
160 newly mature hair cells contained more mature ribbons located at the cell base, below the
161 nucleus (Figure 1E,H, Figure 1-S1C). Overall, our live images examining Riba-TagRFP puncta
162 follows a similar, developmental process as observed in fixed preparations–the number of
163 ribbons and precursors decrease and become basally localized to the presynaptic AZ as the hair
164 cell develops.
165
166 **Microtubule grow plus-ends toward the presynaptic active zone in hair cells**
167 An important question in ribbon formation is how ribbons and precursors migrate to the
168 presynaptic AZ. Work on mouse IHCs using electron microscopy (EM) and super-resolution
169 microscopy found that developing ribbons and precursors often associate with microtubules
170 (Michanski et al., 2019). Similar to what was observed in mice using EM, in living, lateral-line
171 hair cells we observed ribbon precursors associate with microtubules (see yellow arrows in
172 Figure 1F-G). Based on these association studies, a microtubule network may function to
173 transport ribbon precursors during development. To understand if ribbons could be transported
174 along microtubules, we first examined the composition and polarity of the microtubule network
175 in lateral-line hair cells.

176 We first examined the composition, or posttranslational modifications present in the
177 microtubule network in lateral-line hair cells using immunohistochemistry. Using this approach,
178 we labeled either acetylated- (modification found in mechanically stabilized microtubules) or
179 tyrosinated- (modification found in destabilized microtubules) α-tubulin (Janke and Magiera,
180 2020). We performed our staining in a transgenic line that labels all microtubules (*myo6b:YFP-*
181 *tubulin*). We found that in lateral-line hair cells, the microtubule network extends along the
182 apico-basal axis of the cell and is highly acetylated; acetylated microtubules are more
183 concentrated at the cell apex (Figure 2-S1A-C). Outside of the kinocilium, we did not observe a
184 considerable amount of tyrosinated microtubules in lateral-line hair cells. Instead, tyrosinated
185 microtubules were observed in the zebrafish skin, lateral-line nerve terminals and the
186 supporting cells that surround hair cells (Figure 2-S1D-F). Overall, our immunostaining results
187 indicates that in zebrafish lateral-line hair cells, a considerable portion of the microtubule
188 network is highly acetylated. Acetylation could provide a population of mechanically stable
189 microtubules that could be used to transport ribbon precursors.
190 Although microtubule modifications are informative, these labels do not provide
191 definitive information regarding microtubule growth or polarity. Knowing microtubule polarity
192 is important, as many cargos are transported based on polarity. For example, most kinesin
193 motor proteins transport cargos toward the more dynamic plus-end of microtubules (Sweeney
194 and Holzbaur, 2018). Therefore, to explore microtubule polarity in lateral-line hair cells, we
195 created a transgenic line that expresses the plus-end marker of microtubules, EB3 (end-binding
196 protein 3), fused with GFP (example, Figure 2A; *myo6b:EB3-GFP*). Previous work in other cell
197 types has shown that EB3-GFP can be used to visualize the plus-end of growing microtubules
198 (Kawano et al., 2022; Stepanova et al., 2003).
199 We used this transgenic line, along with confocal microscopy to visualize microtubule
200 growth in lateral-line hair cells (z-stacks every 7 s for 20-30 minutes). By imaging EB3-GFP
201 dynamics, we observed comet-like tracks that allowed us to visualize the plus-end of growing
202 microtubules (see Movie S1). In hair cells, microtubule organizing centers are located beneath a
203 single microtubule-based kinocilium, the primary cilium in hair cells (Lepelletier et al., 2013).
204 Consistent with studies in motile cilia, we observed a foci of EB3-GFP at the tips of kinocilia that

205 emanate away from the apex of the cell body (Schrøder et al., 2011) (Figure 2-S2A-C). This
206 result suggests that similar to other cilia, the plus ends of kinocilia are towards their tips, away
207 from the cell body. In addition, we observed EB3-GFP tracks within hair-cell bodies and found
208 that the majority of tracks were directed away from the cell apex and towards the base of the
209 cell (see examples of EB3-GFP timelapse, with tracks rendered into a pseudocolor image based
210 on time; Figure 2C-D). To quantify the direction of EB3-GFP tracks we used Imaris to perform 3D
211 analyses to detect and create vectors of EB3-GFP tracks (see arrows; Figure 2B,E,F). We aligned
212 these vectors along the apico-basal axis of each cell. Here vector movement towards the apex
213 was represented as 180°, and movement to the base was represented at 0° (see schematic,
214 Figure 2G). Movement of EB3-GFP vectors was quantified as the angle between 0 and 180°.
215 From this analysis we found that 77 % of EB3-GFP vectors were directed towards the base in
216 lateral-line hair cells (2006/2598 tracks < 90°, n = 7 neuromasts and 33 hair cells,).
217 Overall, our immunostaining revealed that the soma of hair cells contains a population
218 of microtubules stabilized by acetylation. Our *in vivo* imaging of EB3-GFP revealed that within
219 this population there is extensive microtubules dynamics, and the plus ends of microtubules are
220 primarily directed towards the cell base, and the presynaptic AZ.
221
222 **Ribbon precursors associate with and show directed motion along microtubules**
223 Our analysis of microtubule dynamics using EB3-GFP indicates that the plus ends of
224 microtubules point towards the hair-cell base (Figure 2). Therefore, we hypothesized that these
225 tracks of microtubules could be used by kinesin motor proteins to transport precursors from
226 the cell apex to base during development. To test this hypothesis, we used either Airyscan or
227 Airyscan 2 confocal imaging to capture timelapses of ribbon and precursor movement for
228 longer durations (Airyscan: ~3 µm z-stacks (16-18 slices) every 50-100 s for 30-70 minutes) or
229 for shorter total durations with a faster capture rate (Airyscan 2: ~2-3.5 µm z-stacks (12-20
230 slices) every 20 s for 15-45 minutes). We focused our analysis on developing lateral-line hair
231 cells at early and intermediate stages when ribbon precursors are abundant throughout the cell
232 (Figure 1D,F-G). For this work we used Riba-TagRFP to mark ribbons and precursors, and YFP-
233 tubulin to label microtubules and provide cellular context. From our timelapses, we observed

234 that similar to our initial live analyses (Figure 1F-G), many ribbon precursors associated with
235 microtubules (Movie S2, S3). We also observed that precursors exhibited 3 main movement
236 behaviors related to microtubule association. First, we observed that many precursors
237 associated with microtubules remained stationary or confined (examples: Figure 3C top two
238 panels, Figure 3D,E asterisks, Movie S4). Second, we also observed rapid movement of
239 precursors–during this movement precursors appeared to be in close association with
240 microtubules (examples: Figure 3C bottom 4 panels, Figure 3D,E yellow arrowhead, Figure 3-
241 S1A,B Movie S4, S5). This movement along microtubules occurred bidirectionally, towards the
242 cell apex and towards the base (Figure 3C, middle panels (arrows to base), bottom panels
243 (arrows to apex); Movie S4 (to base), Movie S5 (to apex), Figure 3-S1A-B). Third, we often
244 observed that precursors switched association between neighboring microtubules (Figure 3-
245 S1C, Movie S6).
246 To quantify ribbon and precursor movement, we used Imaris to obtain x,y,z co-ordinates
247 for each ribbon during our timelapses (Longer 30-70 minute acquisitions) (example, Figure 3A-
248 C, Movie S2, S3). This analysis yielded tracks or trajectories for all precursors and ribbons. We
249 then performed a mean-squared displacement (MSD) analysis on ribbon tracks to classify the
250 type of motion we observed. In this analysis, the exponent (α) of MSD vs. time is obtained by
251 curve fitting. A value of $\alpha > 1$ indicates directional motion with velocity, $\alpha = 1$ indicates
252 Brownian motion and $\alpha < 1$ is representative of confined motion or subdiffusion (Figure 3F,G)
253 (Sikora et al., 2017). This method allows us to determine what type of motion each track is
254 exhibiting. Our results show that in developing hair cells, ribbon tracks exhibit directional as
255 well as confined motion (Figure 3H, example MSD tracks with $\alpha < 1$ (red tracks, top panel) and α
256 > 1 (black tracks, bottom panel) from 2 neuromasts). Upon quantification, 19.2 % of ribbon
257 tracks show $\alpha > 1$, indicative of directional motion (n = 7 neuromasts, 30 hair cells and 99
258 tracks). Overall, the vast majority (80.8 %) of ribbon tracks had $\alpha < 1$, indicative of confined
259 motion. Of the tracks that showed directional motion, while the majority move to the cell base,
260 we found that 21.2 % of ribbon tracks moved apically. This apical movement is consistent with a
261 subpopulation of microtubules shows plus-end mediated growth apically (22.8 % of EB3-GFP
262 tracks). Overall, our timelapse imaging demonstrated that ribbons and precursors displayed 3

263 main types of movement on microtubules: confinement, movement along microtubules and
264 switching between microtubules. Further, our MSD analysis indicates that while the majority of
265 precursors exhibit confined motion, a subpopulation of ribbons and precursors exhibit
266 directional motion.
267
268 **Long-term manipulation of microtubules impacts ribbon formation**
269 Our timelapse imaging revealed that precursors and ribbons can move along microtubules in a
270 directional manner. To assess the importance of the microtubule network in ribbon-synapse
271 formation we used pharmacology to destabilize or stabilize the microtubule network in lateral-
272 line hair cells using nocodazole or taxol respectively. We verified the effectiveness of our
273 pharmacological treatments by imaging microtubule dynamics in lateral-line hair cells
274 (*myo6b:YFP-tubulin*). We used Airyscan confocal microscopy to acquire timelapses of YFP-
275 tubulin after a 30-min pharmacological treatment (3 µm z-stacks, every 50-100 s for 30-70 min).
276 These timelapses revealed that compared to controls, 250-500 nM nocodazole and 25 µM taxol
277 dramatically destabilized and stabilized microtubules in lateral-line hair cells (examples see
278 Movie S7). After verifying the effectiveness of our pharmacological treatments, we incubated
279 larvae at 2 dpf for 16 hrs (56-72 hours post fertilization (hpf)), a time window that encompasses
280 a large portion of ribbon-synapse formation in developing hair cells. After these
281 pharmacological treatments we fixed and immunostained larvae to label acetylated-α-tubulin,
282 to monitor changes to the microtubule network. In addition, we co-labeled with Ribeyeb to
283 label ribbons and precursors and pan-Maguk to label postsynapses.
284 After a 16-hr treatment with 250 nM nocodazole we qualitatively observed a decrease
285 in acetylated-α-tubulin label (examples, Figure 4A,C). Less acetylated-α-tubulin label indicates
286 that our nocodazole treatment successfully destabilized microtubules. We also examined the
287 number of hair cells per neuromast and observed that after nocodazole treatment, there were
288 significantly fewer hair cells compared to controls. This indicates that either nocodazole is
289 slightly toxic or it interferes with cell division. Both situations have been observed previously
290 during nocodazole treatments in other systems (Gupta, 1985; Zieve et al., 1980). We next
291 examined the Ribeyeb label in hair cells to assess precursors and ribbons. We observed that the

292 average area of Ribeyeb puncta was significantly reduced compared to controls (Figure 4H).
293 Further, the relative frequency of Ribeyeb puncta with smaller areas was higher in nocodazole
294 treated hair cells compared to controls (Figure 4I). We used cutoff of 0.1 μm^2 to estimate the
295 number of precursors among the Ribeyeb puncta (Figure 4I, > 0.1 μm^2, gray shaded bar
296 encompasses the precursor population). Using this cutoff to identify precursors, we found that
297 there were significantly more precursors per hair cell in nocodazole treatment compared to
298 controls (Figure 4G). We also examined the number of complete synapses (Ribeyeb-Maguk
299 paired puncta) per hair cell after nocodazole treatment. We found that there were significantly
300 fewer complete synapses per hair cell after a 16-hr nocodazole treatment (Figure 4F). Overall,
301 our long-term nocodazole treatment indicated that microtubule destabilization resulted in
302 more ribbons precursors and the formation of fewer synapses per cell.
303 We performed a similar analysis on hair cells after a 16-hr treatment with 25 µM taxol.
304 Qualitatively more acetylated-α-tubulin label was observed after treatment, indicating that our
305 taxol treatment successfully stabilized microtubules (examples, Figure 4-S1A,C). Unlike
306 nocodazole treatment, taxol did not significantly impact the number of hair cells, the average
307 area of Ribeyeb puncta or number of precursors per hair cell compared to controls (Figure 4-
308 S1E,G-H). Interestingly, we observed slightly more complete synapses per hair cell after a 16-hr
309 taxol treatment (Figure 4-S1F). Overall, our long-term taxol treatment indicated that
310 microtubule stabilization did not dramatically impact synapse formation in lateral-line hair cells.
311 Together this pharmacology study revealed that long-term destabilization and
312 stabilization of microtubules during development can impact ribbon formation in lateral-line
313 hair cells. Microtubule destabilization had the most dramatic effect leading to more ribbon
314 precursors and the formation of fewer complete synapses.
315
316 ***Kif1aa* mutants have fewer synapses and more ribbon precursors**
317 In order for cargo (such as ribbons and precursors) to be transported along microtubules,
318 molecular motor proteins are required. Kinesin motor proteins transport cargos along
319 microtubules towards the growing, plus end. Our work demonstrated that in hair cells of the
320 lateral line, the plus-end of microtubules grow from the apex to base of the cell (Figure 2).

321 Single cell RNA sequencing (scRNAseq) has revealed that *kif1aa*, a zebrafish orthologue of Kif1a,
322 a plus-end directed kinesin motor protein, is highly expressed in lateral-line hair cells (Lush et
323 al., 2019). In zebrafish there are 2 orthologues of mammalian *Kif1a*, *kif1aa* and *kif1ab*. While
324 scRNAseq in zebrafish has shown that *kif1ab* and *kif1aa* are widely co-expressed in the nervous
325 system, lateral-line hair cells express just *kif1aa* (Lush et al., 2019; Sur et al., 2023). Therefore,
326 we tested whether Kif1aa could be the kinesin motor that transports ribbons and precursors to
327 the cell base during development.
328 To test for a role of Kif1aa in zebrafish hair cells, we created a CRISPR-Cas9 mutant
329 (Varshney et al., 2016). Our *kif1aa* mutant has a stop codon in the motor domain and is
330 predicted to be a null mutation (Figure 5-S1A-B). For our initial analysis, we co-labeled hair cells
331 at 3 dpf with Ribeyeb to label ribbons and precursors and pan-Maguk to label postsynapses (see
332 examples Figure 5A-D). This is a similar end point used to examine synapse formation after our
333 long-term nocodazole and taxol treatments (Figure 4 and Figure 4-S1). We found that at 3 dpf
334 *kif1aa* mutants had a similar number of hair cells per neuromast (Figure 5E). Despite a similar
335 number of hair cells, we found that there were significantly fewer complete synapses per hair
336 cell in *kif1aa* mutants compared to controls (Figure 5F). In addition, we found that there were
337 significantly more ribbon precursors in *kif1aa* mutants compared to controls (Figure 5G,H,I). As
338 described in the previous section, we also observed fewer complete synapses and more ribbon
339 precursors after a 16-hr nocodazole treatment (Figure 4F,G). Together, this suggests that both
340 intact microtubules and Kif1aa are required for normal ribbon-synapse formation.
341
342 **Short-term disruption of microtubules, but not loss of Kif1aa, impacts ribbon formation**
343 Our initial experiments suggest that microtubule networks and Kif1aa are important for proper
344 ribbon-synapse formation in lateral-line hair cells. But the actual changes in precursors and
345 ribbons within developing hair cells was unclear. Therefore, we examined changes in ribbons
346 and precursors in living lateral-line hair cells over 3-4 hrs of development. For our analysis we
347 used transgenic lines expressing YFP-tubulin to monitor microtubules and Riba-TagRFP to
348 monitor precursors and ribbons *in vivo*. We examined precursors and ribbons after nocodazole
349 or taxol treatment, or after knockdown of Kif1aa during this developmental window.

350 For our pharmacology experiments we first acquired Airyscan confocal images of
351 developing hair cells at 2 dpf that express YFP-tubulin and Riba-TagRFP. Then after a 3-4 hr
352 treatment in either 500 nM nocodazole or 25 µM taxol we reimaged the same hair cells.
353 Consistent with our previous results (Figure 4 and Figure 4-S1) nocodazole and taxol treatments
354 qualitatively destabilized or stabilized microtubules respectively (Figure 6A-F). In each
355 developing cell, we quantified the number of Riba-TagRFP puncta before and after each
356 treatment. In our control samples we observed on average no change in the number of Riba-
357 TagRFP puncta per cell (Figure 6G). Importantly we observed that nocodazole treatment led to
358 a significant increase in the number of Riba-TagRFP puncta over time (Figure 6G). In contrast,
359 similar to controls, taxol treatment did not alter the number of Riba-TagRFP puncta over time
360 (Figure 6G).
361 Next, we used a similar approach to examine the number of Riba-TagRFP puncta in
362 *kif1aa* mutants over a 3-4 hr time window. For this analysis, we examined puncta in *kif1aa* F0
363 crispants. These mutants are derived from injection of 2 *kif1aa* guide RNAs (gRNAs) and Cas9
364 protein. This approach has shown to be an extremely effective way to assay gene function in
365 any genetic background (Hoshijima et al., 2019). Using this approach, we were able to robustly
366 disrupt the *kif1aa* locus. We found that compared to uninjected controls, in *kif1aa* F0 crispants
367 there was no change in the number of Riba-TagRFP puncta per cell over 3-4 hrs (Figure 6-S1A-
368 F). Overall, live imaging over 3-4 hr time windows indicates that a loss of microtubule stability,
369 but not loss of Kif1aa, results in an increase in Riba-TagRFP puncta within developing lateral-line
370 hair cells.
371
372 **Ribbons and precursors require microtubules, but not Kif1aa for directed motion**
373 Our tracking analyses revealed that ribbons and precursors show directed motion on
374 microtubules. Based on these results, we asked what happens to this movement if we disrupt
375 microtubules or the kinesin motor Kif1aa. To test whether microtubules are required for
376 directional ribbon and precursor motion, we used the drugs nocodazole and taxol to alter
377 microtubule dynamics. We treated the fish with these drugs for 30 min and recorded
378 timelapses of ribbon and precursor motion. This short treatment allowed us to observe ribbon

379 motion relatively soon after microtubule disruption and minimize any cytotoxic effects of the
380 compounds. Then we performed MSD analysis on the ribbon tracks to determine if directional
381 motion was impaired (Figure 7A). We found that after destabilizing microtubules by treatment
382 with 500 nM nocodazole for 30 minutes, the proportion of tracks with $\alpha > 1$ was significantly
383 reduced compared to controls (Figure 7C). We also found that the proportion of longer tracks
384 with a cumulative displacement > 1 µm was also reduced after nocodazole treatment compared
385 to controls (Figure 7B,F). This analysis indicates that an intact microtubule network is needed
386 for proper directional ribbon motion and longer displacements. In contrast, after stabilizing
387 microtubules by treatment with 25 µM taxol, we observed no effect on the proportion of tracks
388 with displacement > 1 µm or the proportion of tracks with $\alpha > 1$, compared to controls (Figure
389 7D,G).
390 Next, we used a similar approach to examine the tracks of ribbon and precursor motion
391 in *kif1aa* mutants. For this analysis, we examined ribbon puncta in *kif1aa* F0 crispants. We
392 observed that the proportion of tracks with displacement > 1 µm was not significantly different
393 between *kif1aa* F0 crispants and controls (Figure 7H). Similarly, the proportion of tracks with α
394 > 1, was also not significantly different from the controls (Figure 7H). Overall, these tracking
395 analyses show that in developing lateral-line hair cells, the kinesin motor Kif1aa is not essential
396 for directional motion of ribbons and precursors. In contrast, an unperturbed microtubule
397 network is essential for this directed motion.
398
399 **Ribbon precursors fuse on microtubules**
400 Our analyses demonstrate that movement of ribbon precursors along microtubules is important
401 for synapse formation. But in addition to movement, during development it has been proposed
402 that these small precursors come together or fuse to form larger, more mature ribbons
403 (Michanski et al., 2019). This is consistent with our work, where we see a reduction in ribbon
404 and precursor number alongside development (Figure 1E). Further we see an increase in ribbon
405 and precursor number when microtubules are destabilized (Figure 4), indicating an intact
406 microtubule network may also be important for ribbon fusion.

407 Consistent with this idea, in our timelapses, we observed that ribbons and precursors
408 undergo fusion on microtubules to form larger ribbons. These fusion events occurred between
409 smaller precursors at the cell apex as well as between larger precursors near the cell base
410 (examples: Figure 8A-B, Figure 8-S1A-B, Movies S8-S10). We classified an event as a fusion once
411 the ribbons could not be resolved separately and stayed together for the length of the
412 remaining timelapse (or at least 5 min). These events usually involved ribbon precursors on two
413 separate microtubule filaments coming together during fusion, but fusion events could also
414 occur on the same filament. Although the fusion events were infrequent, within our time
415 windows (30-70 mins), we quantified them and counted an average of 1.7 fusions and a
416 maximum of 5 fusions events per neuromast in developing lateral-line hair cells (n = 27 control
417 neuromasts). Based on the close association with microtubules during these events we tested
418 whether an intact microtubule network was required for fusion events. We found that after
419 treatment with 500 nM nocodazole for 30 minutes, there were fewer fusions events (mean 0.4,
420 maximum 2 fusions per neuromast, n = 10 neuromasts). In contrast, the frequency of fusion
421 events remained unchanged upon treatment with 25 µM taxol for 30 minutes.
422 In our tracking analysis we observed that Kif1aa was not required for directional motion
423 of ribbon and precursors in developing hair cells (Figure 7E,H). But our immunohistological
424 analyses indicated that there are more precursors and fewer complete synapses in *kif1aa*
425 mutants. Therefore, we examined whether Kif1aa was important for fusion events. For this
426 analysis, we quantified fusion events in *kif1aa* F0 crispants. We observed that similar to
427 nocodazole treatment, there were significantly fewer fusions events in *kif1aa* F0 crispants
428 (mean 0.6, maximum 2 fusions per neuromast, n = 9 neuromasts). This reduction in fusion
429 events may ultimately account for the excess of precursors and fewer complete synapses
430 observed in *kif1aa* mutants (Figure 5). Together our results indicate that during development,
431 ribbon precursors can fuse when associated with microtubules and an unperturbed
432 microtubule network, along with Kif1aa is needed for these fusion events.
433
434 **Discussion**

435 Our work in zebrafish applied high resolution imaging approaches to investigate how ribbons
436 are assembled and mobilized in developing hair cells. Our study demonstrates that hair cells
437 have microtubule networks that are polarized with the plus-end pointed to the cell base. Live-
438 imaging approaches highlight that during development, ribbons and precursors show directed
439 motion and fusion along microtubules, and that an intact microtubule network is important for
440 ribbon-synapse formation.
441
442 **Comparison of ribbon synapse formation in zebrafish and mice**
443 Compared to zebrafish hair cells (12-18 hrs), synapse formation and refinement occurs over a
444 relatively long time-window in mouse IHCs (E18-P14). In mice, much of the initial
445 synaptogenesis occurs embryonically, while synapse refinement and pruning occur later,
446 during first postnatal week. Due to the rapid time course of ribbon-synapse development in
447 zebrafish, our experiments likely encompass ribbon precursors movement during
448 synaptogenesis and synapse refinement. Our companion paper on mouse IHCs focused
449 primarily on ribbon mobility during the dramatic pruning of synapses that occurs during early
450 postnatal development (Vorn et al.). Unfortunately, it was not possible to study earlier events
451 in mouse IHCs, as equivalent experiments were not possible embryonically. Live imaging at
452 postnatal stages in mice indicates that during synapse pruning in IHCs, ribbons may detach from
453 the membrane and undergo local trafficking and fuse to nearby presynaptic AZs. Together our
454 studies in zebrafish and mouse hair cells illuminate several common features that characterize
455 ribbon and microtubule dynamics during ribbon-synapse formation.
456 First, immunostaining in both zebrafish and mice revealed an extensive network of
457 microtubules within hair cells. In both species, the majority of microtubules were stabilized by
458 tubulin acetylation (Figure 2-S1). Our *in vivo* imaging of EB3-GFP in zebrafish hair cells revealed
459 that microtubules are very dynamic, and the plus ends of microtubules grow towards the cell
460 base, towards the presynaptic AZ (Figure 2). This data is consistent with data in mouse IHCs
461 demonstrated via immunostaining that the minus end marker of microtubules, CAMSAP2,
462 localizes to the IHC apex (Vorn et. al.). Overall, these studies demonstrate that microtubule
463 networks in developing hair cells are polarized with the plus-end pointed to the cell base.

464 Second, live imaging in zebrafish and mouse hair cells revealed that ribbons associate
465 with and move along microtubules. Tracking and quantification of ribbon movement via MSD
466 analysis revealed that in both zebrafish and mouse hair cells many ribbons show motion
467 indicative of confinement (Figure 3, $\alpha < 1$). In addition, a subset of ribbon tracks show evidence
468 or directed motion (Figure 3, $\alpha > 1$). In both species, after using nocodazole to destabilize
469 microtubules, there was a dramatic reduction in instances of directed motion (Figure 7). In
470 addition to ribbon movement, ribbon fusion was observed in hair cells of mouse and zebrafish
471 (Figure 8). Interestingly in mice many fusion events were balanced out by divisions, or ribbons
472 undergoing separation. In contrast, ribbon divisions were not prevalent in zebrafish hair cells. A
473 lack of ribbon divisions could be due to the rapid speed of development in zebrafish hair cells,
474 where divisions are too transient in nature to be confirmed. Alternatively, divisions may occur
475 primarily late in synapse development and these events were overall less abundant in our
476 zebrafish datasets. Importantly, in both mouse and zebrafish, ribbon fusion was diminished
477 after microtubule destabilization. Together these results in mice and zebrafish demonstrate
478 that an intact microtubule network is required for the directed motion and fusion of ribbons
479 during development.
480 Third, we sought to explore the kinesin motor responsible for ribbon movement in hair
481 cells using zebrafish and mouse models. Based on scRNAseq data and previous immunostaining
482 evidence we focused on Kif1a (Lush et al., 2019; Michanski et al., 2019). In both mouse *Kif1a*
483 and zebrafish *kif1aa* mutants, a common observation was an overall reduction in ribbon
484 volume (Figure 5). This suggests that a conserved mechanism where both intact microtubules
485 and Kif1aa are required for normal ribbon-synapse formation. Despite these results, future
486 work in zebrafish and mice is needed to explore additional kinesin motors that can drive ribbon
487 movement during synapse formation.
488
489 **Fusion on microtubules as a mechanism for ribbon enlargement and maturation**
490 Numerous studies have documented small ribbon precursors in developing photoreceptors and
491 hair cells; later in development there are fewer, large ribbons present (Michanski et al., 2019;
492 Regus-Leidig et al., 2009; Schmitz, 2009; Sheets et al., 2011; Sobkowicz et al., 1986, 1982). This

493 has led to the hypothesis that ribbon precursor fusion is a mechanism to form larger, more
494 mature ribbons (Michanski et al., 2019). Our live imaging experiments show that ribbon fusion
495 is indeed a feature of ribbon formation (Figure 8, Figure 8-S1). Interestingly, we observed that
496 fusion often occurs between precursors on adjacent microtubules. Fusion events can occur
497 both apically and basally within hair cells. More apical fusion events are likely a way to increase
498 ribbon size early in development. More basal fusion events could represent the synapse
499 reduction and refinement that occurs later in synapse development. Whether these later, basal
500 fusion events occur after postsynaptic elements are present is unclear and awaits additional
501 studies. Importantly we found that the number of fusion events is decreased when microtubule
502 networks were disrupted or when Kif1aa was absent (Figure 8). Together these results confirm
503 the hypothesis that ribbons fuse during development. In addition, our work demonstrates that
504 microtubules and Kif1aa are necessary for fusion and may help facilitate this process.
505 Ribbons are aggregates of proteins that share many features with biomolecular
506 condensates that form through liquid–liquid phase separation (LLPS) (Wang et al., 2021).
507 Biomolecular condensates are nano- to micro-meter scale compartments that function to
508 concentrate proteins and nucleic acids. Some examples of biomolecular condensates include
509 tight-junctions, postsynaptic densities, ribonucleoprotein (RNP) granules, and stress granules
510 (Wang et al., 2021; Wiegand and Hyman, 2020). These condensates are highly mobile and
511 dynamic and constituent molecules diffuse readily and exchange with the surrounding
512 environment. Biomolecular condensates often undergo fusion to form larger ones, and then
513 shrink into a spherical shape (Wiegand and Hyman, 2020). FRAP analyses of Ribeye-GFP labeled
514 ribbons in hair cells have confirmed that tagged Ribeye has a fast recovery phase within
515 ribbons, verifying that Ribeye is highly mobile and dynamic within ribbons (Graydon et al.,
516 2017). Further, these FRAP studies revealed that Ribeye molecules can exchange with the
517 surrounding environment. Our present studies confirmed that ribbon precursors undergo
518 fusion to form larger spherical ribbons (Figure 8A,B). Together these studies point towards the
519 idea that precursors and ribbons are indeed biomolecular condensates. Ribeye also contains
520 sequences predicted to be intrinsically disordered, another feature of molecules that can
521 mediate condensate formation. Interestingly, several biomolecular condensates such as RNP

522 transport granules are known to be transported along the microtubules (Knowles at al., 1996),
523 similar to our observations of ribbon precursor transport.
524 In our current study we also found that microtubules are needed for fusion (Figure 8C).
525 In other cellular contexts, the energy released by dynamic microtubules via growth and
526 shrinkage can be used for force generation in a wide range of processes (Vleugel et al., 2016).
527 Interestingly work on stress granules condensates, found a connection between dynamic
528 microtubules and stress granule formation. This work demonstrated that microtubule growth
529 and shrinkage promoted the fusion of small cytoplasmic granules into larger ones (Chernov et
530 al., 2009). In addition, this study also demonstrated that stress granules slide along
531 microtubules, and that this movement may act in conjunction with pushing or pulling to
532 promote fusion (Chernov et al., 2009). Similar interactions could occur between ribbons and
533 microtubules during development to promote fusion. Disruption of microtubules would then
534 destabilize the formation of larger ribbons. This is consistent with our results, where we
535 observed in more precursors and fewer mature ribbon synapses after nocodazole treatment
536 (Figure 4F,G).
537 We also observed that fusion was disrupted in *kif1aa* mutants, despite finding that
538 directed transport of precursors and ribbons remained unchanged in *kif1aa* mutants (Figure
539 7,8). A recent study on RNP condensates examined kinesin motors and adaptors in the context
540 of microtubules (Cochard et al., 2023). This work found that the precise combination of motor
541 proteins or adaptors can impact where condensates form. Some combinations enabled the
542 formation and transport of condensates along microtubules. But other combinations restricted
543 condensate formation to microtubule terminals where motor proteins are predicted to form a
544 scaffold. Our work indicates that while more than one kinesin motor protein is capable of
545 transporting ribbons precursors, it is predominantly Kif1aa that mediates fusion along
546 microtubules. This could explain why precursor fusion, but not transport is impacted in *kif1aa*
547 mutants (Figure 7,8). This scenario could also explain the extra precursors and fewer complete
548 synapses that form in *kif1aa* mutants over time (Figure 5).
549
550 **Kinesin motors and adaptors for ribbon transport on microtubules**

551 Our immunohistochemistry analyses show clear synaptic defects in *kif1aa* mutants after the
552 bulk of synapse formation has occurred (fewer synapses, more precursors, Figure 5). Despite
553 these defects, we were unable to demonstrate that loss of Kif1aa impacts the movement of
554 precursors along microtubules (Figure 7). These results suggests that another kinesin motor
555 may function to transport precursors and ribbons. Pulldown assay have shown an interaction of
556 Kif3a with Ribeye (Uthaiah and Hudspeth, 2010). While *kif1aa* mRNA is the most abundant
557 kinesin motor protein transcript detected in lateral-line hair cells, *kif3a* mRNA is also present.
558 *Kif3a* mRNA is present at lower levels and is expressed more broadly in lateral-line hair cells,
559 supporting cells and afferent neurons (Sur et al., 2023). Therefore, it is possible that both Kif1aa
560 and Kif3a are competent to transport developing ribbons. Future work exploring the role of
561 Kif3a separately or in combination with Kif1aa will illuminate the role these motors play in hair-
562 cell synapse assembly.
563 Regardless of the anterograde kinesin motor(s) that transports precursors to the cell
564 base, we also observed that precursors can also move in the retrograde direction, towards the
565 cell apex (Figure 3C bottom panels and Figure 3-S1B). In fact, out of the tracks with directional
566 motion, we found that 21.2 % of precursor tracks moved apically. This could be due to the fact
567 that a subpopulation of microtubules shows plus-end mediated growth apically (22.8 %).
568 Alternatively, it is possible that retrograde motors may also transport ribbon precursors. For
569 example, this could be accomplished using minus-end directed motors, such as cytoplasmic
570 dynein heavy chain, or kinesins in the kinesin-14 family (Sweeney and Holzbaur, 2018; Yamada
571 et al., 2017). In the future it will be important to explore the role of these additional motor
572 proteins in the context of ribbon and precursor mobility.
573 It is clear from our work that ribbons and precursors show directed motion indicative of
574 motor-mediated transport (Figure 3 and 7). An important part of transport is adaptor proteins
575 that selectively link cargos to specific motor proteins (Fu and Holzbaur, 2014). In neurons,
576 cargos leave the Golgi apparatus and are packed into specialized transport vesicles, along with
577 adaptor scaffolds (Farías et al., 2012; Sampo et al., 2003). Work in neurons has shown that the
578 Kif1a motor transports Rab3-positive synaptic vesicle precursors (Okada et al., 1995). This
579 transport is thought to rely on DENN (differentially expressed in normal and neoplastic

580 cells)/MADD (MAP kinase activating death domain) which links synaptic vesicle precursors to
581 Kif1a (Hummel and Hoogenraad, 2021; Niwa et al., 2008). Interesting, like mature ribbons,
582 ribbon precursors are decorated with synaptic vesicles (Michanski et al., 2019). Thus, is it
583 possible that these synaptic vesicles may contain adaptor proteins that couple the ribbon to a
584 kinesin motor to enable transport. In the future it will be important to identify this adaptor
585 protein, and to understand what other molecules are co-transported with Ribeye during ribbon
586 formation.
587
588 **Ribbon formation in the absence of microtubules**
589 Our work indicates that over short time scales (30-70 mins), when microtubules are destabilized
590 via nocodazole treatment, fewer ribbons and precursors show directed motion indicative of
591 active transport (Figure 7). In addition, when hair cells are treated with nocodazole for the
592 entire duration of development (16 hrs) fewer synapses form (Figure 4). But in both of these
593 treatment paradigms, some ribbons still show directed motion, and some synapses still form,
594 even when microtubules are disrupted. If tracks of microtubules are required for developing
595 precursors and ribbons mobility during development what underlies this residual movement
596 and synapse formation?
597 One possibility is that not all microtubules are disrupted after nocodazole treatment.
598 Nocodazole treatment can be cytotoxic, especially at doses high enough to eliminate all
599 microtubules (~40 µM) (Laisne et al., 2021). The nocodazole doses we tested were not cytotoxic
600 (100-500 nM), although higher doses did result in death of hair cells. At these lower doses it
601 was difficult to eliminate all microtubules, especially those located more apically, which appear
602 to be extremely stable (example, Figure 2-S1). It is possible that the residual ribbon mobility
603 observed during nocodazole treatment occurs along these remaining microtubules.
604 Alternatively, it is possible that other filaments such as actin or intermediate filaments may also
605 play a role or aid in ribbon mobility. Work in mouse IHC has shown that actin filaments are
606 required to regulate and organize synaptic vesicles at mature ribbon synapses (Guillet et al.,
607 2016). In addition, in mice, the actin-based motor protein Myosin6 has been shown to localize
608 to ribbons and loss of Myosin6 impacts ribbon-synapse number and function (Roux et al.,

609 2009). In addition, it is possible that ribbons and precursors may also move throughout the cell
610 via diffusion and localize to the active zone via a 'capture' mechanism through an adapter
611 protein. Although we primarily see ribbons and precursors attached to microtubules, when
612 these filaments are destabilized using nocodazole, movement could still occur via diffusion.
613 Once the ribbons diffuse towards the base, other presynaptic molecules, such as Bassoon,
614 could act to anchor ribbons at the active zone (Jing et al., 2013). Any of these scenarios could
615 explain how ribbons move and how synapses form when microtubules are destabilized. In all
616 likelihood, transport along microtubules, other cytoskeletal filaments, and diffusive movement
617 are all required to ensure that ribbon synapses form properly. Additional pharmacology and
618 imaging experiments are needed to delineate between these possibilities.
619
620 **Does spontaneous activity shape ribbon transport or fusion?**
621 In previous work we demonstrated that spontaneous calcium activity impacts ribbon formation
622 in zebrafish hair cells (Sheets et al., 2012; Wong et al., 2019). Spontaneous activity is well
623 documented in developing sensory systems [reviewed in: (Leighton and Lohmann, 2016)]. In
624 the inner ear of mammals, spontaneous activity in sensory hair cells is thought to act during
625 development to establish neuronal connections within the inner ear, and to act downstream in
626 the brain to shape tonotopic maps (Ceriani et al., 2019; Tritsch et al., 2007). In our previous
627 work in lateral-line hair cells, we found that spontaneous rises in presynaptic-calcium loads
628 calcium into synaptic mitochondria. Calcium loading into the mitochondria regulates the mount
629 of NAD^+ to NAD(H) in the developing hair cell. Blocking either presynaptic or mitochondria
630 calcium during development results in higher levels of NAD^+, the formation of larger ribbons,
631 fewer synapses, and the retention of small ribbon precursors in hair cells (Sheets et al., 2012;
632 Wong et al., 2019). What aspect of ribbon formation is impacted by spontaneous activity
633 remains unclear.
634 Work in yeast has shown that calcium is important for microtubule stability (Adamíková
635 et al., 2004; Façanha et al., 2002). In addition, work in dendritic spines has shown that synaptic
636 calcium responses promote microtubule entry into active spines (Merriam et al., 2013).
637 Therefore, it is possible that spontaneous calcium activity may act to stabilize microtubules or

638 facilitate movement to the presynaptic AZ to facilitate ribbon transport. In addition to altering
639 the microtubule network, spontaneous activity could also impact ribbon fusion. Protein
640 condensate formation and fusion is influenced by many aspects of the cellular environment,
641 including temperature, pH, osmolarity and ion concentration (Wang et al., 2022). Elevated
642 calcium can promote the fusion of chromogranin proteins that undergo LLPS in the Golgi lumen
643 (Gerdes et al., 1989; Yoo, 1995). Therefore, it is possible that elevated calcium during a
644 spontaneous calcium event could promote ribbon or precursor fusion. In addition to the cellular
645 environment, posttranslational modifications to the proteins within the condensate can impact
646 formation and LLPS. Such modifications include: phosphorylation, acetylation, SUMOylation,
647 ubiquitination, methylation, and ADP-ribosylation (Luo et al., 2021). These modifications can
648 alter protein-protein interactions by changing the charge, structure, or hydrophobicity. Our
649 previous work implicated that NAD^+ or NAD(H) via a NAD^+/NADH binding domain on Ribeye,
650 could impact ribbon formation (Wong et al., 2019). It is possible that in addition to calcium,
651 NAD^+/NADH levels in the cell could modify Ribeye to facilitate condensate formation or fusion.
652 In the future it will be important to use the live imaging approaches outlined here to
653 understand how spontaneous presynaptic- and mitochondrial-calcium influx impact the
654 movement and fusion of ribbon precursors.
655
656 Overall, our live imaging studies demonstrate that microtubule networks are critical for ribbon
657 and precursor mobility, and fusion in developing zebrafish hair cells. But ribbon synapses
658 contain many molecules, and synapse formation requires many successive steps. In the future it
659 will be important to develop approaches to tag and label other presynaptic ($Ca_V1.3$ channels,
660 Bassoon, Piccolino) and postsynaptic proteins (PSD95, GluR2) that make up ribbon synapses.
661 For this future work, zebrafish is an ideal model system for creating these new genetic tools and
662 for live imaging studies. By imaging ribbons, along with these other tagged synaptic
663 components, we will gain a more comprehensive picture of ribbon-synapse formation.
664 Understanding how ribbon synapses form is essential to determine how to reform synapses
665 when they are disrupted in auditory and visual disorders.
666

667 **Methods**

668 **Zebrafish animals**

669 Zebrafish (*Danio rerio*) were bred and cared for at the National Institutes of Health (NIH) under
670 animal study protocol #1362-13. Zebrafish larvae raised at 28°C in E3 embryo medium (5 mM
671 NaCl, 0.17 mM KCl, 0.33 mM $CaCl_2$, and 0.33 mM $MgSO_4$, buffered in HEPES, pH 7.2). All
672 experiments were performed on larvae aged 2-3 days post fertilization (dpf). Larvae were
673 chosen at random at an age where sex determination is not possible. The previously described
674 mutant and transgenic lines were used in this study: *Tg(myo6b:ctbp2a-TagRFP)*^{idc11Tg} referred to
675 as *myo6b:riba-TagRFP; Tg(myo6b:YFP-Hsa.TUBA)*^{idc16Tg} referred to as *myo6b:YFP-tubulin* (Ohta
676 et al., 2020; Wong et al., 2019).

677

678 **Zebrafish transgenic and CRISPR-Cas9 mutant generation**

679 To create *myo6b:EB3-GFP* transgenic fish, plasmid construction was based on the tol2/gateway
680 zebrafish kit (Kwan et al., 2007). The p5E *pmyo6b* entry clone (Trapani et al., 2009) was used to
681 drive expression in hair cells. A pME-*EB3-GFP* clone was kindly provided by Catherine Drerup at
682 University of Wisconsin, Madison. pDestTol2pACryGFP was a gift from Joachim Berger & Peter
683 Currie (Addgene plasmid # 64022). These clones were used along with the following tol2 kit
684 gateway clone, p3E-*polyA* (#302) to create the expression construct: *myo6b:EB3-GFP*. To
685 generate the stable transgenic fish line *myo6b:EB3-GFP*^{idc23Tg}, plasmid DNA and tol2
686 transposase mRNA were injected into zebrafish embryos as previously described (Kwan et al.,
687 2007). The *myo6b:EB3-GFP*^{idc23Tg} transgenic line was selected for single copy and low expression
688 of EB3-GFP.

689 A *kif1aa* germline mutant was generated in-house using CRISPR-Cas9 technology as
690 previously described (Varshney et al., 2016). Exon 6, containing part of the Kinesin motor
691 domain was targeted. Guides RNAs (gRNAs) targeted to *kif1aa* are as follows: 5'-
692 ACGGATGTTCTCGCACACGT(AGG)-3', 5'-GTGCGAGAACATCCGTTGCT(AGG)-3', 5'-
693 TGGACTCCGGGAATAAGGCT(AGG)-3', 5'-AGAATACCTAGCCTTATTCC(CGG)-3'. Founder fish were
694 identified using fragment analysis of fluorescent PCR (fPCR) products. A founder fish containing
695 a complex INDEL that destroys a BslI restriction site in exon 6 was selected (Figure 5-S1B). This

696 INDEL disrupts the protein at amino acid 166 (Figure 5-S1A). Subsequent genotyping was
697 accomplished using standard PCR and Bsl1 restriction enzyme digestion. *Kif1aa* genotyping
698 primers used were: *kif1aa*_FWD 5'-AACACCAAGCTGACCAGTGC-3' and *kif1aa*_REV 5'-
699 TGCGGTCCTAGGCTTACAAT-3'.
700 We created *kif1aa* F0 crispants for our live imaging analyses. Here we injected the
701 following *kif1aa* gRNAs: 5'-GTGCGAGAACATCCGTTGCT(AGG)-3' and 5'-
702 AGAATACCTAGCCTTATTCC(CGG)-3', along with Cas9 protein, as previously described (Hoshijima
703 et al., 2019). We then grew *kif1aa* injected F0 crispants for 2 days and then used them for our
704 live imaging analyses. Because *kif1aa* mutants have no phenotype to distinguish them from
705 sibling controls at the ages imaged, the low throughput of our live imaging approaches made
706 using germline mutants prohibitive. Studies have shown that F0 crispants are a fast and
707 effective way to knockdown gene function in any genetic background (Hoshijima et al., 2019;
708 Sheets et al., 2021). After live imaging, we genotyped all *kif1aa* F0 crispants to ensure that the
709 gRNAs cut the target robustly using fragment analysis of fluorescent PCR products and the
710 following primers: *kif1aa*_FWD_fPCR 5'-TGTAAAACGACGGCCAGT-
711 AAATAGAGATTCACTTTTAATC-3' and *kif1aa*_REV_fPCR 5'- GTGTCTT-
712 CCTAGGCTTACAATGCTTTTGG-3' (Carrington et al., 2015). Any *kif1aa* F0 crispants without
713 robust genomic cutting were not included in analyses.
714
715 **Zebrafish pharmacology**
716 To destabilize or stabilize microtubules, larval zebrafish at 2 dpf were incubated in either
717 nocodazole (Sigma-Aldrich, SML1665) or Paclitaxel (taxol) (Sigma-Aldrich, 5082270001). Both
718 drugs were maintained in DMSO. For experiments these drugs were diluted in media for a final
719 concentration of 0.1 % DMSO, 250-500 nM nocodazole and 25 µM taxol. For controls, larvae
720 were incubated in media containing 0.1 % DMSO. For long-term incubation (16 hr), wild-type
721 larvae were incubated in E3 media containing 250 nM nocodazole or 25 µM taxol at 54 hpf for
722 16 hrs (overnight). After this long-term treatment, larvae were fixed and prepared for
723 immunohistochemistry (see below). For live, short-term incubations (for 3-4 hr incubations or
724 ribbon tracking), transgenic larvae (*myo6b:riba-tagRFP; Tg(myo6b:YFP-alpha-tubulin*) at 48-54

725 hpf were embedded in 1 % low melt agarose prepared in E3 media containing 0.03 % tricaine
726 (Sigma-Aldrich, A5040, ethyl 3-aminobenzoate methanesulfonate salt). 500 nM nocodazole, 25
727 µM taxol or DMSO were added to the agarose and to the E3 media used to hydrate the sample.
728 For these short-term treatments, hair cells were imaged after 30 min of embedding.
729
730 **Immunohistochemistry of zebrafish samples**
731 Immunohistochemistry to label acetylated-tubulin, tyrosinated-tubulin, Ribeyeb (ribbons and
732 precursors), pan-Maguk (postsynaptic densities) and Myosin7a (hair-cell bodies) was performed
733 on whole zebrafish larvae similar to previous work. The following primary antibodies were
734 used: rabbit anti-Myosin7a (Proteus 25-6790; 1:1000) mouse anti-pan-Maguk (IgG1) (Millipore
735 MABN7; 1:500); mouse anti-Ribeyeb (IgG2a) ((Sheets et al., 2011); 1:10,000); mouse anti-
736 acetylated-tubulin (IgG2b) (Sigma-Aldrich T7451; 1:5,000); mouse anti-tyrosinated-tubulin
737 (IgG2a) (Sigma-Aldrich MAB1864-I; 1:1,000); chicken anti-GFP (to stain YFP-tubulin) (Aves labs
738 GFP-1010; 1:1,000). The following secondary antibodies were used at 1:1,000: (ThermoFisher
739 Scientific, A-11008; A-21143, A-21131, A-21240; A-11-039, A-21242, A-21241, A-11039). Larvae
740 were fixed with 4 % paraformaldehyde in PBS for 4 hr at 4°C. All wash, block and antibody
741 solutions were prepared in 0.1 % Tween in PBS (PBST). After fixation, larvae were washed 5 × 5
742 min in PBST. Prior to block, larvae were permeabilized with acetone. For this permeabilization
743 larvae were first washed for 5 min with H_2O. The H_2O was removed and replaced with ice-cold
744 acetone and placed at −20°C for 3 min, followed by a 5 min H_2O wash. The larvae were then
745 washed for 5 × 5 min in PBST. Larvae were then blocked overnight at 4°C in blocking solution (2
746 % goat serum, 1 % bovine serum albumin, 2 % fish skin gelatin in PBST). Larvae were then
747 incubated in primary antibodies in antibody solution (1 % bovine serum albumin in PBST)
748 overnight, nutating at 4°C. The next day, the larvae were washed for 5 × 5 min in PBST to
749 remove the primary antibodies. Secondary antibodies in antibody solution were added and
750 larvae were incubated for 3 hrs at room temperature. After 5 × 5 min washes min in PBST to
751 remove the secondary antibodies, larvae were rinsed in H_2O and mounted in Prolong gold
752 (ThermoFisher Scientific P36930).
753

754 **Confocal imaging and analysis of fixed zebrafish samples**

755 After immunostaining, fixed zebrafish samples were imaged on an inverted Zeiss LSM 780 (Zen
756 2.3 SP1) or an upright Zeiss LSM 980 (Zen 3.4) laser-scanning confocal microscope with Airyscan
757 using a 63x 1.4 NA oil objective lens. Z-stacks encompassing the entire neuromast were
758 acquired every 0.17 (LSM 980) or 0.18 (LSM 780) µm with an 0.04 µm x-y pixel size and Airyscan
759 autoprocessed in 3D.

760 Synaptic images from fixed samples were further processed using FIJI. Acetylated
761 tubulin or Myosin7 label was used to manually count hair cells. Complete synapses comprised
762 of both a Ribeyeb and Maguk puncta were also counted manually. To quantify ribbon and
763 precursor areas, images were processed in a FIJI
764 'IJMacro_AIRYSCAN_simple3dSeg_noco_ribbons only.ijm' as previously described (Wong et al.,
765 2019). Here each Airyscan z-stack was max-projected. Background was subtracted from each
766 projection using rolling-ball subtraction. A threshold was applied to each image, followed by
767 segmentation to delineate individual Ribeyeb puncta. The watershed function was used to
768 separate adjacent puncta. A list of 2D objects of individual ROIs (minimum size filter of 0.002
769 μm^2) was created to measure the areas of Ribeyeb puncta. Areas for all Ribeyeb puncta within
770 each neuromast were then exported as a csv spreadsheet. For comparisons, all fixed images
771 analyzed in FIJI were imaged and processed using the same parameters.

772

773 **Confocal imaging and *in vivo* analysis of ribbon numbers in developing zebrafish hair cells**

774 For counting ribbon numbers in developing and mature hair cells (Figure 1), double transgenic
775 *myo6b:riba-TagRFP* and *myo6b:YFP-tubulin* larvae at 2 and 3 dpf were imaged. Transgenic
776 larvae were pinned to a Sylgard-filled petri dish in E3 media containing 0.03 % tricaine and
777 imaged on a Nikon A1R upright confocal microscope using a 60x 1 NA water objective lens.
778 Denoised images were acquired using NIS Elements AR 5.20.02 with an 0.425 µm z-interval, at,
779 16x averaging, and 0.05 µm/pixel. Z-stacks of whole neuromasts including the kinocilium were
780 acquired in a top-down configuration using 488 and 561 nm lasers. The 488 nm laser along with
781 a transmitted PMT (T-PMT) detector was used to capture the kinocilial heights.

782 For quantification of ribbon numbers at different hair-cell developmental stages (Figure
783 1), a custom-written Fiji macro "Live ribbon counter" was used to batch-process the z-stacks.
784 The red channel (Riba-TagRFP) of each z-stack was thresholded (threshold value = 97).
785 Watershed was applied to the thresholded stack to separate ribbons near each other. The
786 resulting mask from the thresholding and watershedding was applied to the original red
787 channel. The number of ribbons was then counted using '3D Objects Counter' (Threshold = 1,
788 min size = 0, max size = 183500). The counted objects were merged with the green channel
789 (YFP-tubulin). Each z-stack was visually inspected to determine the localization of the ribbons.
790 Ribbons below the nucleus were classified as 'basal' and the rest as 'apical'. The number of
791 apical and basal ribbons were counted in each hair cell.
792 To classify the developmental stage of each hair cell (Figure 1), the height of the
793 kinocilium was used. The number of z-slices between the kinocilium tip and base was
794 determine and multiplied by the z-slice interval (0.425 µm) to get the kinocilium height. Hair
795 cells with heights < 2.5 µm were classified as 'Early', hair cells with heights 2.5-10 µm were
796 classified as 'Intermediate' and with heights 10-18 µm were classified as 'Late'. Hair cells with
797 heights > 18 µm were considered 'Mature'.
798
799 **Confocal imaging and *in vivo* tracking EB3-GFP dynamics in zebrafish**
800 Transgenic *myo6b:EB3-GFP* larvae at 2-3 dpf were mounted in 1 % LMP agarose containing 0.03
801 % tricaine in a glass-bottom dish. Larvae were imaged on an inverted Zeiss LSM 780 (Zen 2.3
802 SP1) confocal microscope using a 63x 1.4 NA oil objective lens. For timelapses, confocal z-stacks
803 of partial cell volumes (3.5 µm, 7 z slices at 0.5 µm z interval) with an 0.07 µm x-y pixel size
804 were taken every 7 s for 15-30 min.
805 The EB3-GFP timelapses were tracked in Imaris. For spot detection, we used an
806 estimated xy diameter of 0.534 µm with background subtraction. The detected spots were
807 filtered by 'Quality' using the automatic threshold. The timelapses were visually checked to
808 make sure the spot detection was accurate. For the tracking step, the 'Autoregressive motion'
809 algorithm was used, with a maximum linking distance of 1 µm and a maximum gap size of 3

810 frames. To ensure accurate track detection, short tracks were removed by filtering for the
811 number of spots in a track (> 5) and track displacement length (> automatic threshold).
812 To calculate the track angles relative to the hair-cell base, we used cells that lie
813 horizontally so we only need to consider the angles in the xy place. In Imaris, the tracks in each
814 hair cell were selected and exported separately. Using the start and end position co-ordinates
815 of the exported tracks, we calculated track angles in MATLAB using custom written code called,
816 "EB3 track angle". The angle of each hair cell was measured in Imaris. The final track angle
817 distribution plotted was obtained by measuring the difference between each track angle and
818 the angle of the hair cell.
819 To create movies of EB3-GFP tracks in Movie S1, the FIJI plugin TrackMate was used
820 (Tinevez et al., 2017). For Movie S1, the LoG detector in TrackMate was used with an estimated
821 object diameter of 0.6 µm, a quality threshold of 8, using a median filter and sub-pixel
822 localization. The Linear Assignment Problem (LAP) tracker was selected using frame to frame
823 linking max distance of 1 µm, a track segment gap closing max distance of 1 µm and max frame
824 gap of 2 µm. Tracks were colored by Track index. For viewing tracks over time, tracks were
825 displayed as "Show tracks backwards in time" with a fade range of 5 time-points. To create
826 color-coded temporal map of EB3-GFP tracks over a short time window (21 s, Figure 2C-D), the
827 FIJI Hyperstack plugin Temporal-Color code was used with the 16 colors LUT.
828
829 **Confocal imaging and *in vivo* analysis of ribbon numbers after short-term pharmacological**
830 **treatments in zebrafish**
831 For counting ribbons after 3-4 hr drug treatment, transgenic zebrafish expressing *myo6b:riba-*
832 *TagRFP* and *myo6b:YFP-tubulin* at 2 dpf were examined. Transgenic larvae were mounted in 1 %
833 low melt agarose in E3 media containing 0.03 % tricaine and one of the following: 500 nM
834 nocodazole, 25 µM taxol or 0.1 % DMSO (Control). An inverted Zeiss LSM 780 (Zen 2.3 SP1)
835 confocal microscope with Airyscan, along with a 63x NA 1.4 oil objective lens. Z-stacks
836 encompassing the entire neuromast were acquired every or 0.18 µm with an 0.04 µm x-y pixel
837 size and Airyscan autoprocessed in 3D.

838 To quantification of ribbon numbers before and after 3-4 hr nocodazole and taxol
839 treatment or in *kif1aa* F0 crispants (Figure 6, Figure 6-S1), the custom-written Fiji macro "Live
840 ribbon counter" described above was used to batch-processed the z-stacks. The red channel
841 (Riba-TagRFP) of each z-stack was thresholded (threshold value = 28) and segmented
842 (watershed). The resulting mask was applied to the original red channel. The number of ribbons
843 was then counted using '3D Objects Counter' (threshold = 1, min size = 0, max size = 183500).
844 The counted objects were merged with the green channel (YFP-tubulin). Each z-stack was
845 visually inspected to make sure the objects counted were within hair cells. The number of
846 ribbons per neuromast was determined and the difference in numbers pre- and post-drug
847 treatment was plotted.
848
849 **Confocal imaging and *in vivo* tracking of ribbons**
850 To visualize ribbon precursor movement, timelapses of double transgenic *myo6b:riba-TagRFP*
851 and *myo6b:YFP-tubulin* larvae at 2 dpf were imaged. For pharmacological treatments,
852 transgenic larvae were mounted in 1 % low melt agarose in E3 media containing 0.03 % tricaine
853 and one of the following: 500 nM nocodazole, 25 µM taxol or 0.1 % DMSO (Control) in a glass-
854 bottom dish. Double transgenic *kif1aa* crispants and uninjected controls were mounted in 1 %
855 low melt agarose in E3 media containing 0.03 % tricaine in a glass-bottom dish. Larvae were
856 imaged on an inverted Zeiss LSM 780 or an upright LSM 980 confocal microscope with Airyscan
857 using a 63x 1.4 NA oil objective lens. Airyscan z-stacks of partial cell volumes (~3 µm, 16-18 z-
858 slices using 0.18 µm z-interval and an 0.04 µm x-y pixel size) were taken on the LSM 780 every
859 50-100 s for 30-70 min. Faster LSM 980 Airscan z-stacks of partial cell volumes (~2-3.5 µm, 12-
860 20 z-slices using 0.17 µm z interval and an 0.04 µm x-y pixel size) were taken every 20 s for 15-
861 45 min. Airyscan timelapses were autoprocessed in 3D. In addition, we acquired a subset of
862 LSM 780 Airscan z-stacks every 5-8 min for 30-100 min to capture fusion events more for clearly
863 for Movies S8-10.
864 The longer timelapses acquired on the Zeiss LSM 780 were tracked in Imaris using spot
865 detection with estimated xy diameters of 0.427 µm (with background subtraction). The spots
866 were filtered based on 'Quality', with thresholds between 3-8, chosen after visual inspection of

867 the detected spots. For tracking, the 'Autoregressive motion' algorithm was used with a
868 maximum linking distance of 1.13 µm and a maximum gap size of 3 frames. Tracks with number
869 of spots < 5 were not included. Using the Track displacement length filter in Imaris, the number
870 of tracks with Track displacement length > 1 µm were counted and divided by the total number
871 of tracks to get the fractions plotted in Figure 7. For the mean squared displacement (MSD)
872 analysis, the xyzt co-ordinates were exported in 'csv' format for all tracks in a timelapse. The
873 MSD analysis was done using the prewritten MATLAB class MSDanalyzer (Tarantino et al.,
874 2014). MSDanalyzer calculates the mean squared displacement for each track, curve-fits the
875 MSD vs time, and provides the value of the exponent (α). The first 25 % of the MSD vs time
876 graph was used for curve-fitting. Tracks with the number of spots < 10 were removed to ensure
877 accuracy of the MSD analysis.

878 **Statistics**

879 All data shown are mean ± standard error of the mean (SEM). All zebrafish experiments were
880 compiled from data acquired on at least two independent days from different clutches. All
881 replicates were biological–distinct animals and cells. Wild-type animals were selected at
882 random for drug treatments. Datasets were excluded if there was excessive x-y-or z drift. In all
883 datasets dot plots represent the 'n'. N represents either the number of neuromasts, hair cells,
884 synapses or puncta as stated in the legends. For all zebrafish experiments a minimum of 3
885 animals and 6 neuromasts were examined. Sample sizes were selected to avoid Type 2 error. All
886 statistical analyses were performed using Prism 10 software (GraphPad). A D'Agostino-Pearson
887 normality test was used to test for normal distributions. To test for statistical significance
888 between two samples, either unpaired t-tests (normally distributed data), or Wilcoxon or
889 Mann-Whitney tests (not normally distributed data) were used. A p-value less than 0.05 was
890 considered significant.

891 **Contributions**

892 KK, SH and H-TW did the immunohistochemistry, along with the imaging and analysis of fixed
893 samples. KP and MU created the *kif1aa* mutants. KP created *kif1aa* cripants for analyses and

894 made the *myo6b:EB3-GFP* transgenic line. SH did all the live imaging, along with the
895 quantifications and tracking analyses. KK and SH made figures and wrote the manuscript.
896
897 **Data Availability Statement**
898 All data and code used in this paper will be available on Dyrad upon revision.
899
900 **Acknowledgements**
901 We thank Juan Angueyra and Katie Drerup for their comments on our manuscript. This work
902 was supported by National Institute on Deafness and Other Communication Disorders (NIDCD)
903 Intramural Research Program Grant 1ZIADC000085-01 (KK) and Project B08 of the Collaborative
904 Research Center 889 '*Cellular Mechanisms of Sensory Processing*' of the German Research
905 Foundation (MU, awarded to Christian Vogl).
906
907
908 **References**
909 Adamíková L, Straube A, Schulz I, Steinberg G. 2004. Calcium Signaling Is Involved in Dynein-
910 dependent Microtubule Organization. *Mol Biol Cell* **15**:1969–1980.
911 doi:10.1091/mbc.E03-09-0675
912 Ahmari SE, Buchanan J, Smith SJ. 2000. Assembly of presynaptic active zones from cytoplasmic
913 transport packets. *Nat Neurosci* **3**:445–451. doi:10.1038/74814
914 Brandt A, Striessnig J, Moser T. 2003. CaV1.3 channels are essential for development and
915 presynaptic activity of cochlear inner hair cells. *J Neurosci* **23**:10832–10840.
916 Bury LAD, Sabo SL. 2011. Coordinated trafficking of synaptic vesicle and active zone proteins
917 prior to synapse formation. *Neural Develop* **6**:24. doi:10.1186/1749-8104-6-24
918 Carrington B, Varshney GK, Burgess SM, Sood R. 2015. CRISPR-STAT: an easy and reliable PCR-
919 based method to evaluate target-specific sgRNA activity. *Nucleic Acids Res* **43**:e157.
920 doi:10.1093/nar/gkv802
921 Ceriani F, Hendry A, Jeng J-Y, Johnson SL, Stephani F, Olt J, Holley MC, Mammano F, Engel J,
922 Kros CJ, Simmons DD, Marcotti W. 2019. Coordinated calcium signalling in cochlear
923 sensory and non-sensory cells refines afferent innervation of outer hair cells. *EMBO J*
924 **38**:e99839. doi:10.15252/embj.201899839
925 Chang B, Heckenlively JR, Bayley PR, Brecha NC, Davisson MT, Hawes NL, Hirano AA, Hurd RE,
926 Ikeda A, Johnson BA, Mccall MA, Morgans CW, Nusinowitz S, Peachey NS, Rice DS,
927 Vessey KA, Gregg RG. 2006. The nob2 mouse, a null mutation in Cacna1f: Anatomical
928 and functional abnormalities in the outer retina and their consequences on ganglion cell
929 visual responses. *Vis Neurosci* **23**:11–24. doi:10.1017/S095252380623102X

930 Chernov KG, Barbet A, Hamon L, Ovchinnikov LP, Curmi PA, Pastré D. 2009. Role of
931 microtubules in stress granule assembly. *J Biol Chem* **284**:36569–36580.
932 doi:10.1074/jbc.M109.042879
933 Cochard A, Safieddine A, Combe P, Benassy M-N, Weil D, Gueroui Z. 2023. Condensate
934 functionalization with microtubule motors directs their nucleation in space and allows
935 manipulating RNA localization. *EMBO J* **n/a**:e114106. doi:10.15252/embj.2023114106
936 Dick O, tom Dieck S, Altrock WD, Ammermüller J, Weiler R, Garner CC, Gundelfinger ED,
937 Brandstätter JH. 2003. The presynaptic active zone protein bassoon is essential for
938 photoreceptor ribbon synapse formation in the retina. *Neuron* **37**:775–786.
939 doi:10.1016/s0896-6273(03)00086-2
940 Dow E, Siletti K, Hudspeth AJ. 2015. Cellular projections from sensory hair cells form polarity-
941 specific scaffolds during synaptogenesis. *Genes Dev* **29**:1087–1094.
942 doi:10.1101/gad.259838.115
943 Façanha ALO, Appelgren H, Tabish M, Okorokov L, Ekwall K. 2002. The endoplasmic reticulum
944 cation P-type ATPase Cta4p is required for control of cell shape and microtubule
945 dynamics. *J Cell Biol* **157**:1029–1039. doi:10.1083/jcb.200111012
946 Farías GG, Cuitino L, Guo X, Ren X, Jarnik M, Mattera R, Bonifacino JS. 2012. Signal-mediated,
947 AP-1/clathrin-dependent sorting of transmembrane receptors to the somatodendritic
948 domain of hippocampal neurons. *Neuron* **75**:810–823.
949 doi:10.1016/j.neuron.2012.07.007
950 Fejtova A, Davydova D, Bischof F, Lazarevic V, Altrock WD, Romorini S, Schöne C, Zuschratter W,
951 Kreutz MR, Garner CC, Ziv NE, Gundelfinger ED. 2009. Dynein light chain regulates
952 axonal trafficking and synaptic levels of Bassoon. *J Cell Biol* **185**:341–355.
953 doi:10.1083/jcb.200807155
954 Frank T, Rutherford MA, Strenzke N, Neef A, Pangršič T, Khimich D, Fejtova A, Gundelfinger ED,
955 Liberman MC, Harke B, Bryan KE, Lee A, Egner A, Riedel D, Moser T. 2010. Bassoon and
956 the synaptic ribbon organize Ca^2+ channels and vesicles to add release sites and
957 promote refilling. *Neuron* **68**:724–738. doi:10.1016/j.neuron.2010.10.027
958 Frederick CE, Zenisek D. 2023. Ribbon synapses and retinal disease: review. *Int J Mol Sci*
959 **24**:5090. doi:10.3390/ijms24065090
960 Freeman W. 1928. The function of the lateral line organs. *Science* **68**:205–205.
961 doi:10.1126/science.68.1757.205
962 Fu M, Holzbaur ELF. 2014. Integrated regulation of motor-driven organelle transport by
963 scaffolding proteins. *Trends Cell Biol* **24**:564–574. doi:10.1016/j.tcb.2014.05.002
964 Gerdes HH, Rosa P, Phillips E, Baeuerle PA, Frank R, Argos P, Huttner WB. 1989. The primary
965 structure of human secretogranin II, a widespread tyrosine-sulfated secretory granule
966 protein that exhibits low pH- and calcium-induced aggregation. *J Biol Chem* **264**:12009–
967 12015. doi:10.1016/S0021-9258(18)80167-3
968 Graydon CW, Manor U, Kindt KS. 2017. In vivo ribbon mobility and turnover of Ribeye at
969 zebrafish hair cell synapses. *Sci Rep* **7**:7467. doi:10.1038/s41598-017-07940-z
970 Guillet M, Sendin G, Bourien J, Puel J-L, Nouvian R. 2016. Actin Filaments Regulate Exocytosis at
971 the Hair Cell Ribbon Synapse. *J Neurosci* **36**:649–654. doi:10.1523/JNEUROSCI.3379-
972 15.2016

973 Gundelfinger ED, Reissner C, Garner CC. 2016. Role of bassoon and piccolo in assembly and
974 molecular organization of the active zone. *Front Synaptic Neurosci* **7**:19.
975 doi:10.3389/fnsyn.2015.00019
976 Gupta RS. 1985. Species-specific differences in toxicity of antimitotic agents toward cultured
977 mammalian cells2. *JNCI J Natl Cancer Inst* **74**:159–164. doi:10.1093/jnci/74.1.159
978 Hoshijima K, Jurynec MJ, Klatt Shaw D, Jacobi AM, Behlke MA, Grunwald DJ. 2019. Highly
979 efficient crispr-cas9-based methods for generating deletion mutations and f0 embryos
980 that lack gene function in zebrafish. *Dev Cell* **51**:645-657.e4.
981 doi:10.1016/j.devcel.2019.10.004
982 Hummel JJA, Hoogenraad CC. 2021. Specific KIF1A-adaptor interactions control selective cargo
983 recognition. *J Cell Biol* **220**:e202105011. doi:10.1083/jcb.202105011
984 Janke C, Magiera MM. 2020. The tubulin code and its role in controlling microtubule properties
985 and functions. *Nat Rev Mol Cell Biol* **21**:307–326. doi:10.1038/s41580-020-0214-3
986 Jean P, Lopez de la Morena D, Michanski S, Jaime Tobón LM, Chakrabarti R, Picher MM, Neef J,
987 Jung S, Gültas M, Maxeiner S, Neef A, Wichmann C, Strenzke N, Grabner C, Moser T.
988 2018. The synaptic ribbon is critical for sound encoding at high rates and with temporal
989 precision. *eLife* **7**:e29275. doi:10.7554/eLife.29275
990 Jia S, Muto A, Orisme W, Henson HE, Parupalli C, Ju B, Baier H, Taylor MR. 2014. Zebrafish
991 Cacna1fa is required for cone photoreceptor function and synaptic ribbon formation.
992 *Hum Mol Genet* **23**:2981–2994. doi:10.1093/hmg/ddu009
993 Jing Z, Rutherford MA, Takago H, Frank T, Fejtova A, Khimich D, Moser T, Strenzke N. 2013.
994 Disruption of the presynaptic cytomatrix protein bassoon degrades ribbon anchorage,
995 multiquantal release, and sound encoding at the hair cell afferent synapse. *J Neurosci*
996 **33**:4456–67. doi:10.1523/JNEUROSCI.3491-12.2013
997 Kawano D, Pinter K, Chlebowski M, Petralia RS, Wang Y-X, Nechiporuk AV, Drerup CM. 2022.
998 NudC regulated Lis1 stability is essential for the maintenance of dynamic microtubule
999 ends in axon terminals. *iScience* **25**:105072. doi:10.1016/j.isci.2022.105072
1000 Khimich D, Nouvian R, Pujol R, Tom Dieck S, Egner A, Gundelfinger ED, Moser T. 2005. Hair cell
1001 synaptic ribbons are essential for synchronous auditory signalling. *Nature* **434**:889–894.
1002 doi:10.1038/nature03418
1003 Kindt KS, Finch G, Nicolson T. 2012. Kinocilia mediate mechanosensitivity in developing
1004 zebrafish hair cells. *Dev Cell* **23**:329–341. doi:10.1016/j.devcel.2012.05.022
1005 Kujawa SG, Liberman MC. 2015. Synaptopathy in the noise-exposed and aging cochlea: primary
1006 neural degeneration in acquired sensorineural hearing loss. *Hear Res* **330**:191–199.
1007 doi:10.1016/j.heares.2015.02.009
1008 Kwan KM, Fujimoto E, Grabher C, Mangum BD, Hardy ME, Campbell DS, Parant JM, Yost HJ,
1009 Kanki JP, Chien C-B. 2007. The Tol2kit: a multisite gateway-based construction kit for
1010 Tol2 transposon transgenesis constructs. *Dev Dyn Off Publ Am Assoc Anat* **236**:3088–
1011 3099. doi:10.1002/dvdy.21343
1012 Laisne M-C, Michallet S, Lafanechère L. 2021. Characterization of microtubule destabilizing
1013 drugs: a quantitative cell-based assay that bridges the gap between tubulin based- and
1014 cytotoxicity assays. *Cancers* **13**:5226. doi:10.3390/cancers13205226

1015 Leighton AH, Lohmann C. 2016. The wiring of developing sensory circuits-from patterned
1016 spontaneous activity to synaptic plasticity mechanisms. *Front Neural Circuits* **10**:71.
1017 doi:10.3389/fncir.2016.00071
1018 Lepelletier L, de Monvel JB, Buisson J, Desdouets C, Petit C. 2013. Auditory hair cell centrioles
1019 undergo confined brownian motion throughout the developmental migration of the
1020 kinocilium. *Biophys J* **105**:48–58. doi:10.1016/j.bpj.2013.05.009
1021 Luo Y-Y, Wu J-J, Li Y-M. 2021. Regulation of liquid–liquid phase separation with focus on post-
1022 translational modifications. *Chem Commun* **57**:13275–13287. doi:10.1039/D1CC05266G
1023 Lush ME, Diaz DC, Koenecke N, Baek S, Boldt H, St Peter MK, Gaitan-Escudero T, Romero-
1024 Carvajal A, Busch-Nentwich EM, Perera AG, Hall KE, Peak A, Haug JS, Piotrowski T. 2019.
1025 scRNA-Seq reveals distinct stem cell populations that drive hair cell regeneration after
1026 loss of Fgf and Notch signaling. *eLife* **8**:e44431. doi:10.7554/eLife.44431
1027 Maas C, Torres VI, Altrock WD, Leal-Ortiz S, Wagh D, Terry-Lorenzo RT, Fejtova A, Gundelfinger
1028 ED, Ziv NE, Garner CC. 2012. Formation of Golgi-derived active zone precursor vesicles. *J*
1029 *Neurosci* **32**:11095–11108. doi:10.1523/JNEUROSCI.0195-12.2012
1030 Magupalli VG, Schwarz K, Alpadi K, Natarajan S, Seigel GM, Schmitz F. 2008. Multiple RIBEYE-
1031 RIBEYE interactions create a dynamic scaffold for the formation of synaptic ribbons. *J*
1032 *Neurosci* **28**:7954–7967. doi:10.1523/JNEUROSCI.1964-08.2008
1033 Mansergh F, Orton NC, Vessey JP, Lalonde MR, Stell WK, Tremblay F, Barnes S, Rancourt DE,
1034 Bech-Hansen NT. 2005. Mutation of the calcium channel gene Cacna1f disrupts calcium
1035 signaling, synaptic transmission and cellular organization in mouse retina. *Hum Mol*
1036 *Genet* **14**:3035–3046. doi:10.1093/hmg/ddi336
1037 Maxeiner S, Luo F, Tan A, Schmitz F, Südhof TC. 2016. How to make a synaptic ribbon: RIBEYE
1038 deletion abolishes ribbons in retinal synapses and disrupts neurotransmitter release.
1039 *EMBO J* **35**:1098–1114. doi:10.15252/embj.201592701
1040 Merriam EB, Millette M, Lumbard DC, Saengsawang W, Fothergill T, Hu X, Ferhat L, Dent EW.
1041 2013. Synaptic regulation of microtubule dynamics in dendritic spines by calcium, F-
1042 actin, and drebrin. *J Neurosci* **33**:16471–16482. doi:10.1523/JNEUROSCI.0661-13.2013
1043 Michanski S, Kapoor R, Steyer AM, Möbius W, Früholz I, Ackermann F, Gültas M, Garner CC,
1044 Hamra FK, Neef J, Strenzke N, Moser T, Wichmann C. 2023. Piccolino is required for
1045 ribbon architecture at cochlear inner hair cell synapses and for hearing. *EMBO Rep*
1046 **n/a**:e56702. doi:10.15252/embr.202256702
1047 Michanski S, Smaluch K, Steyer AM, Chakrabarti R, Setz C, Oestreicher D, Fischer C, Möbius W,
1048 Moser T, Vogl C, Wichmann C. 2019. Mapping developmental maturation of inner hair
1049 cell ribbon synapses in the apical mouse cochlea. *Proc Natl Acad Sci* **116**:6415–6424.
1050 doi:10.1073/pnas.1812029116
1051 Nemzou N. RM, Bulankina AV, Khimich D, Giese A, Moser T. 2006. Synaptic organization in
1052 cochlear inner hair cells deficient for the CaV1.3 (α1D) subunit of L-type Ca2+ channels.
1053 *Neuroscience* **141**:1849–1860. doi:10.1016/j.neuroscience.2006.05.057
1054 Niwa S, Tanaka Y, Hirokawa N. 2008. KIF1Bβ- and KIF1A-mediated axonal transport of
1055 presynaptic regulator Rab3 occurs in a GTP-dependent manner through DENN/MADD.
1056 *Nat Cell Biol* **10**:1269–1279. doi:10.1038/ncb1785
1057 Obholzer N, Wolfson S, Trapani JG, Mo W, Nechiporuk A, Busch-Nentwich E, Seiler C, Sidi S,
1058 Söllner C, Duncan RN, Boehland A, Nicolson T. 2008. Vesicular glutamate transporter 3 is

1059 required for synaptic transmission in zebrafish hair cells. *J Neurosci* **28**:2110–2118.
1060 doi:10.1523/JNEUROSCI.5230-07.2008
1061 Ohta S, Ji YR, Martin D, Wu DK. 2020. Emx2 regulates hair cell rearrangement but not positional
1062 identity within neuromasts. *eLife*. doi:10.7554/eLife.60432
1063 Okada Y, Yamazaki H, Sekine-Aizawa Y, Hirokawa N. 1995. The neuron-specific kinesin
1064 superfamily protein KIF1A is a unique monomeric motor for anterograde axonal
1065 transport of synaptic vesicle precursors. *Cell* **81**:769–780. doi:10.1016/0092-
1066 8674(95)90538-3
1067 Oliver D, Ramachandran S, Philbrook A, Lambert CM, Nguyen KCQ, Hall DH, Francis MM. 2022.
1068 Kinesin-3 mediated axonal delivery of presynaptic neurexin stabilizes dendritic spines
1069 and postsynaptic components. *PLoS Genet* **18**:e1010016.
1070 doi:10.1371/journal.pgen.1010016
1071 Pack-Chung E, Kurshan PT, Dickman DK, Schwarz TL. 2007. A Drosophila kinesin required for
1072 synaptic bouton formation and synaptic vesicle transport. *Nat Neurosci* **10**:980–989.
1073 doi:10.1038/nn1936
1074 Regus-Leidig H, Fuchs M, Löhner M, Leist SR, Leal-Ortiz S, Chiodo VA, Hauswirth WW, Garner
1075 CC, Brandstätter JH. 2014. In vivo knockdown of Piccolino disrupts presynaptic ribbon
1076 morphology in mouse photoreceptor synapses. *Front Cell Neurosci* **8**.
1077 Regus-Leidig H, tom Dieck S, Specht D, Meyer L, Brandstätter JH. 2009. Early steps in the
1078 assembly of photoreceptor ribbon synapses in the mouse retina: The involvement of
1079 precursor spheres. *J Comp Neurol* **512**:814–824. doi:10.1002/cne.21915
1080 Roux I, Hosie S, Johnson SL, Bahloul A, Cayet N, Nouaille S, Kros CJ, Petit C, Safieddine S. 2009.
1081 Myosin VI is required for the proper maturation and function of inner hair cell ribbon
1082 synapses. *Hum Mol Genet* **18**:4615–4628. doi:10.1093/hmg/ddp429
1083 Ruel J, Emery S, Nouvian R, Bersot T, Amilhon B, Van Rybroek JM, Rebillard G, Lenoir M, Eybalin
1084 M, Delprat B, Sivakumaran TA, Giros B, El Mestikawy S, Moser T, Smith RJH, Lesperance
1085 MM, Puel J-L. 2008. Impairment of SLC17A8 encoding vesicular glutamate transporter-3,
1086 VGLUT3, underlies nonsyndromic deafness DFNA25 and inner hair cell dysfunction in
1087 null mice. *Am J Hum Genet* **83**:278–292. doi:10.1016/j.ajhg.2008.07.008
1088 Sampo B, Kaech S, Kunz S, Banker G. 2003. Two distinct mechanisms target membrane proteins
1089 to the axonal surface. *Neuron* **37**:611–624. doi:10.1016/s0896-6273(03)00058-8
1090 Schmitz F. 2009. The making of synaptic ribbons: how they are built and what they do. *Neurosci*
1091 *Rev J Bringing Neurobiol Neurol Psychiatry* **15**:611–624.
1092 doi:10.1177/1073858409340253
1093 Schmitz F, Königstorfer A, Südhof TC. 2000. RIBEYE, a component of synaptic ribbons: a
1094 protein's journey through evolution provides insight into synaptic ribbon function.
1095 *Neuron* **28**:857–872. doi:10.1016/S0896-6273(00)00159-8
1096 Schrøder JM, Larsen J, Komarova Y, Akhmanova A, Thorsteinsson RI, Grigoriev I, Manguso R,
1097 Christensen ST, Pedersen SF, Geimer S, Pedersen LB. 2011. EB1 and EB3 promote cilia
1098 biogenesis by several centrosome-related mechanisms. *J Cell Sci* **124**:2539–2551.
1099 doi:10.1242/jcs.085852
1100 Shapira M, Zhai RG, Dresbach T, Bresler T, Torres VI, Gundelfinger ED, Ziv NE, Garner CC. 2003.
1101 Unitary assembly of presynaptic active zones from Piccolo-Bassoon transport vesicles.
1102 *Neuron* **38**:237–252. doi:10.1016/s0896-6273(03)00207-1

1103 Sheets L, Holmgren M, Kindt KS. 2021. How zebrafish can drive the future of genetic-based
1104 hearing and balance research. *JARO J Assoc Res Otolaryngol* **22**:215–235.
1105 doi:10.1007/s10162-021-00798-z
1106 Sheets L, Kindt KS, Nicolson T. 2012. Presynaptic CaV1.3 channels regulate synaptic ribbon size
1107 and are required for synaptic maintenance in sensory hair cells. *J Neurosci* **32**:17273–
1108 17286. doi:10.1523/JNEUROSCI.3005-12.2012
1109 Sheets L, Trapani JG, Mo W, Obholzer N, Nicolson T. 2011. Ribeye is required for presynaptic
1110 Ca(V)1.3a channel localization and afferent innervation of sensory hair cells. *Dev Camb*
1111 *Engl* **138**:1309–1319. doi:10.1242/dev.059451
1112 Sikora G, Teuerle M, Wyłomańska A, Grebenkov D. 2017. Statistical properties of the
1113 anomalous scaling exponent estimator based on time-averaged mean-square
1114 displacement. *Phys Rev E* **96**:022132. doi:10.1103/PhysRevE.96.022132
1115 Sobkowicz HM, Rose JE, Scott GE, Slapnick SM. 1982. Ribbon synapses in the developing intact
1116 and cultured organ of Corti in the mouse. *J Neurosci* **2**:942–957.
1117 doi:10.1523/JNEUROSCI.02-07-00942.1982
1118 Sobkowicz HM, Rose JE, Scott GL, Levenick CV. 1986. Distribution of synaptic ribbons in the
1119 developing organ of Corti. *J Neurocytol* **15**:693–714. doi:10.1007/BF01625188
1120 Stepanova T, Slemmer J, Hoogenraad CC, Lansbergen G, Dortland B, Zeeuw CID, Grosveld F,
1121 Cappellen G van, Akhmanova A, Galjart N. 2003. Visualization of microtubule growth in
1122 cultured neurons via the use of eb3-gfp (end-binding protein 3-green fluorescent
1123 protein). *J Neurosci* **23**:2655–2664. doi:10.1523/JNEUROSCI.23-07-02655.2003
1124 Suli A, Watson GM, Rubel EW, Raible DW. 2012. Rheotaxis in larval zebrafish is mediated by
1125 lateral line mechanosensory hair cells. *PLoS ONE* **7**. doi:10.1371/journal.pone.0029727
1126 Sur A, Wang Y, Capar P, Margolin G, Prochaska MK, Farrell JA. 2023. Single-cell analysis of
1127 shared signatures and transcriptional diversity during zebrafish development. *Dev Cell*
1128 **58**:3028-3047.e12. doi:10.1016/j.devcel.2023.11.001
1129 Sweeney HL, Holzbaur ELF. 2018. Motor Proteins. *Cold Spring Harb Perspect Biol* **10**:a021931.
1130 doi:10.1101/cshperspect.a021931
1131 Tarantino N, Tinevez J-Y, Crowell EF, Boisson B, Henriques R, Mhlanga M, Agou F, Israël A,
1132 Laplantine E. 2014. TNF and IL-1 exhibit distinct ubiquitin requirements for inducing
1133 NEMO–IKK supramolecular structures. *J Cell Biol* **204**:231–245.
1134 doi:10.1083/jcb.201307172
1135 Tinevez J-Y, Perry N, Schindelin J, Hoopes GM, Reynolds GD, Laplantine E, Bednarek SY, Shorte
1136 SL, Eliceiri KW. 2017. TrackMate: An open and extensible platform for single-particle
1137 tracking. *Methods*, Image Processing for Biologists **115**:80–90.
1138 doi:10.1016/j.ymeth.2016.09.016
1139 Trapani JG, Obholzer N, Mo W, Brockerhoff SE, Nicolson T. 2009. Synaptojanin1 is required for
1140 temporal fidelity of synaptic transmission in hair cells. *PLOS Genet* **5**:e1000480.
1141 doi:10.1371/journal.pgen.1000480
1142 Tritsch NX, Yi E, Gale JE, Glowatzki E, Bergles DE. 2007. The origin of spontaneous activity in the
1143 developing auditory system. *Nature* **450**:50–55. doi:10.1038/nature06233
1144 Uthaiah RC, Hudspeth AJ. 2010. Molecular anatomy of the hair cell's ribbon synapse. *J Neurosci*
1145 **30**:12387–12399. doi:10.1523/JNEUROSCI.1014-10.2010

1146 Varshney GK, Carrington B, Pei W, Bishop K, Chen Z, Fan C, Xu L, Jones M, LaFave MC, Ledin J,
1147 Sood R, Burgess SM. 2016. A high-throughput functional genomics workflow based on
1148 CRISPR/Cas9-mediated targeted mutagenesis in zebrafish. *Nat Protoc* **11**:2357–2375.
1149 doi:10.1038/nprot.2016.141
1150 Vleugel M, Kok M, Dogterom M. 2016. Understanding force-generating microtubule systems
1151 through in vitro reconstitution. *Cell Adhes Migr* **10**:475–494.
1152 doi:10.1080/19336918.2016.1241923
1153 Wang B, Zhang Lei, Dai T, Qin Z, Lu H, Zhang Long, Zhou F. 2021. Liquid–liquid phase separation
1154 in human health and diseases. *Signal Transduct Target Ther* **6**:1–16.
1155 doi:10.1038/s41392-021-00678-1
1156 Wang Z, Lou J, Zhang H. 2022. Essence determines phenomenon: Assaying the material
1157 properties of biological condensates. *J Biol Chem* **298**. doi:10.1016/j.jbc.2022.101782
1158 Wiegand T, Hyman AA. 2020. Drops and fibers — how biomolecular condensates and
1159 cytoskeletal filaments influence each other. *Emerg Top Life Sci* **4**:247–261.
1160 doi:10.1042/ETLS20190174
1161 Wong HC, Zhang Q, Beirl AJ, Petralia RS, Wang Y-X, Kindt K. 2019. Synaptic mitochondria
1162 regulate hair-cell synapse size and function. *eLife* **8**:e48914. doi:10.7554/eLife.48914
1163 Yamada M, Tanaka-Takiguchi Y, Hayashi M, Nishina M, Goshima G. 2017. Multiple kinesin-14
1164 family members drive microtubule minus end–directed transport in plant cells. *J Cell Biol*
1165 **216**:1705–1714. doi:10.1083/jcb.201610065
1166 Yoo SH. 1995. pH- and Ca2+-induced Conformational Change and Aggregation of Chromogranin
1167 B.: COMPARISON WITH CHROMOGRANIN A AND IMPLICATION IN SECRETORY VESICLE
1168 BIOGENESIS (*). *J Biol Chem* **270**:12578–12583. doi:10.1074/jbc.270.21.12578
1169 Zhang Q, Kindt KS. 2022. Using light-sheet microscopy to study spontaneous activity in the
1170 developing lateral-line system. *Front Cell Dev Biol* **10**:819612.
1171 doi:10.3389/fcell.2022.819612
1172 Zieve GW, Turnbull D, Mullins JM, McIntosh JR. 1980. Production of large numbers of mitotic
1173 mammalian cells by use of the reversible microtubule inhibitor nocodazole. Nocodazole
1174 accumulated mitotic cells. *Exp Cell Res* **126**:397–405. doi:10.1016/0014-4827(80)90279-
1175 7
1176

1177

1178

1179

1180

1181

1182 **Figures and Legends**

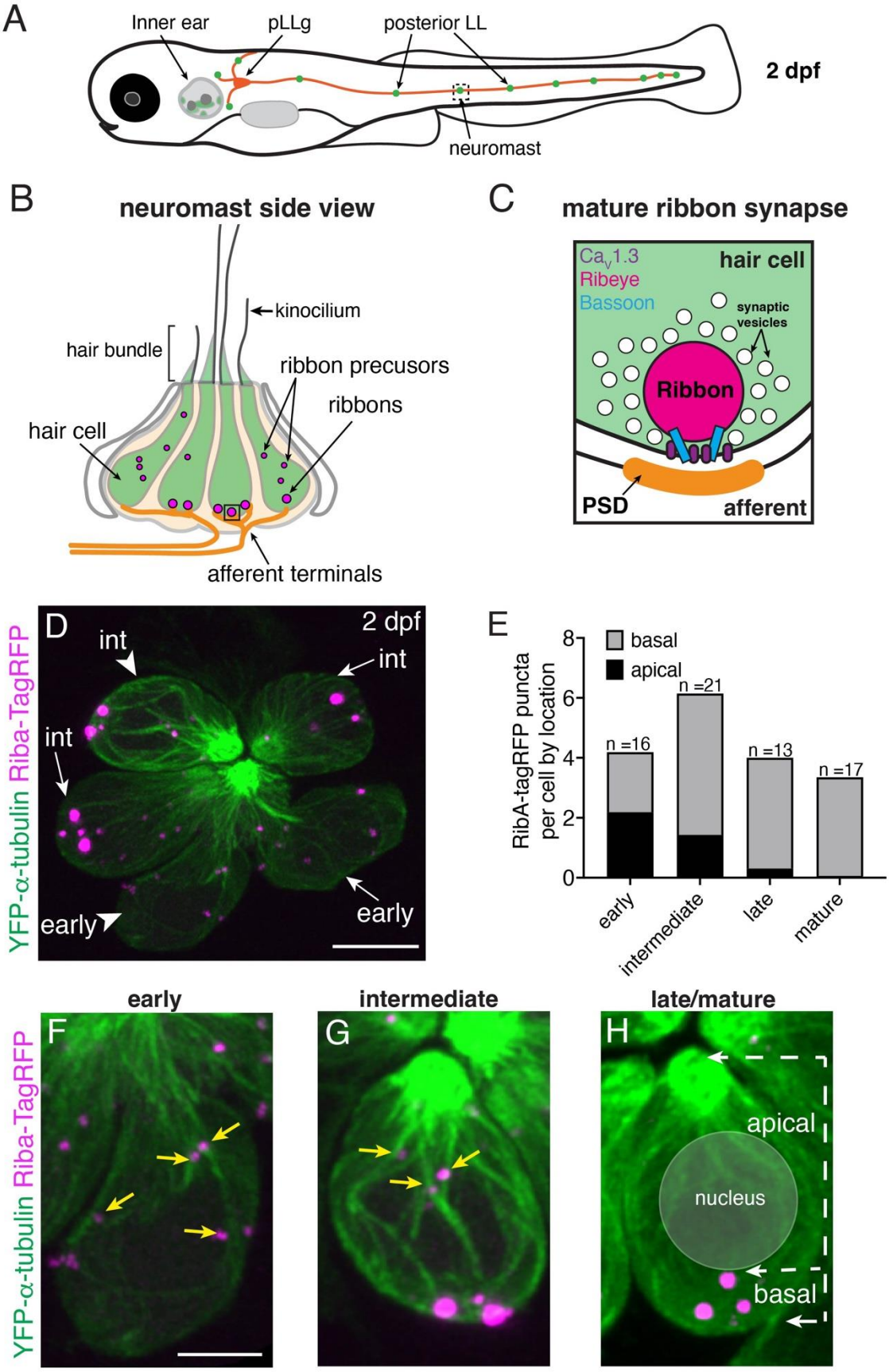
A
Inner ear
pLLg
posterior LL
2 dpf
neuromast
B
neuromast side view
kinocilium
hair bundle
ribbon precusors
ribbons
hair cell
afferent terminals
C
mature ribbon synapse
Cav1.3
Ribeye
Bassoon
hair cell
synaptic vesicles
Ribbon
PSD
afferent
D
2 dpf
int
int
int
early
early
YFP-α-tubulin Riba-TagRFP
E
basal
apical
RibA-tagRFP puncta per cell by location
n =16
n =21
n =13
n =17
early
intermediate
late
mature
early
intermediate
late/mature
F
G
H
YFP-α-tubulin Riba-TagRFP
apical
nucleus
basal

1183

1184 **Figure 1 – Ribbons associate with microtubules and change localization during development**
1185 **A)** Schematic of a larval zebrafish at 2 days post fertilization (dpf) with the location of the
1186 posterior-lateral line (LL) indicated relative to the zebrafish inner ear. Neuromasts (green) in the
1187 posterior LL contain sensory hair cells that are innervated by afferent projections from the
1188 posterior LL ganglion (pLLg, orange). **B)** Schematic of a neuromast at 2 dpf, viewed from the
1189 side. At 2 dpf, the majority of hair cells (green) are developing. A shorter kinocilium (part of the
1190 mechanosensory hair bundle) and an abundance of small ribbon precursors are indicative of an
1191 immature stage. **C)** Schematic of a ribbon synapse when mature. The dense presynapse or
1192 ribbon is made primarily of Ribeye. Ribbons tether synaptic vesicles near $Ca_V1.3$ channels at the
1193 plasma membrane, across from the postsynaptic density (PSD). Bassoon acts to anchor ribbons
1194 at the presynaptic AZ. **D)** Example image of a neuromast at 2 dpf, viewed from top down. The
1195 microtubule network and ribbons are marked with YFP-Tubulin and Riba-TagRFP respectively. In
1196 this example of 6 developing hair cells, 2 early and 4 intermediate cells are present. The cell
1197 bodies of an early and intermediate cell from this example (arrowheads) are expanded in **F** and
1198 **G**. **E)** Plot shows the average number of ribbons per hair cell at each developmental stage. Cell
1199 stage is determined by the height of the kinocilium. After an increase in ribbon number with
1200 development, there is a decrease upon maturation. The number of apically-localized Riba-
1201 TagRFP puncta is high at early and intermediate stages, and is lower in late and mature hair
1202 cells. In contrast, the number of basally-localized Riba-TagRFP puncta is low at early stages, and
1203 becomes higher by intermediate stages (n = 16, 21, 13, 17 hair cells for early, intermediate, late
1204 and mature stages respectively). **F-H)** Example images of hair cells expressing YFP-Tubulin and
1205 Riba-TagRFP at early, intermediate and late stages. At the early stage, Riba-TagRFP puncta are
1206 spread throughout the cell body and are smaller in size. At the intermediate stage, the number
1207 of Riba-TagRFP puncta become more basally enriched and appear larger in size. In late and
1208 mature hair cells, all Riba-TagRFP puncta are at the base of the cell and fewer in number. The
1209 arrows in **H** highlight the apical and basal region of the cell used for quantification of Riba-
1210 TagRFP puncta location in **E**. Scale bars in **D** = 5 µm and in **F** = 2 µm.
1211
1212

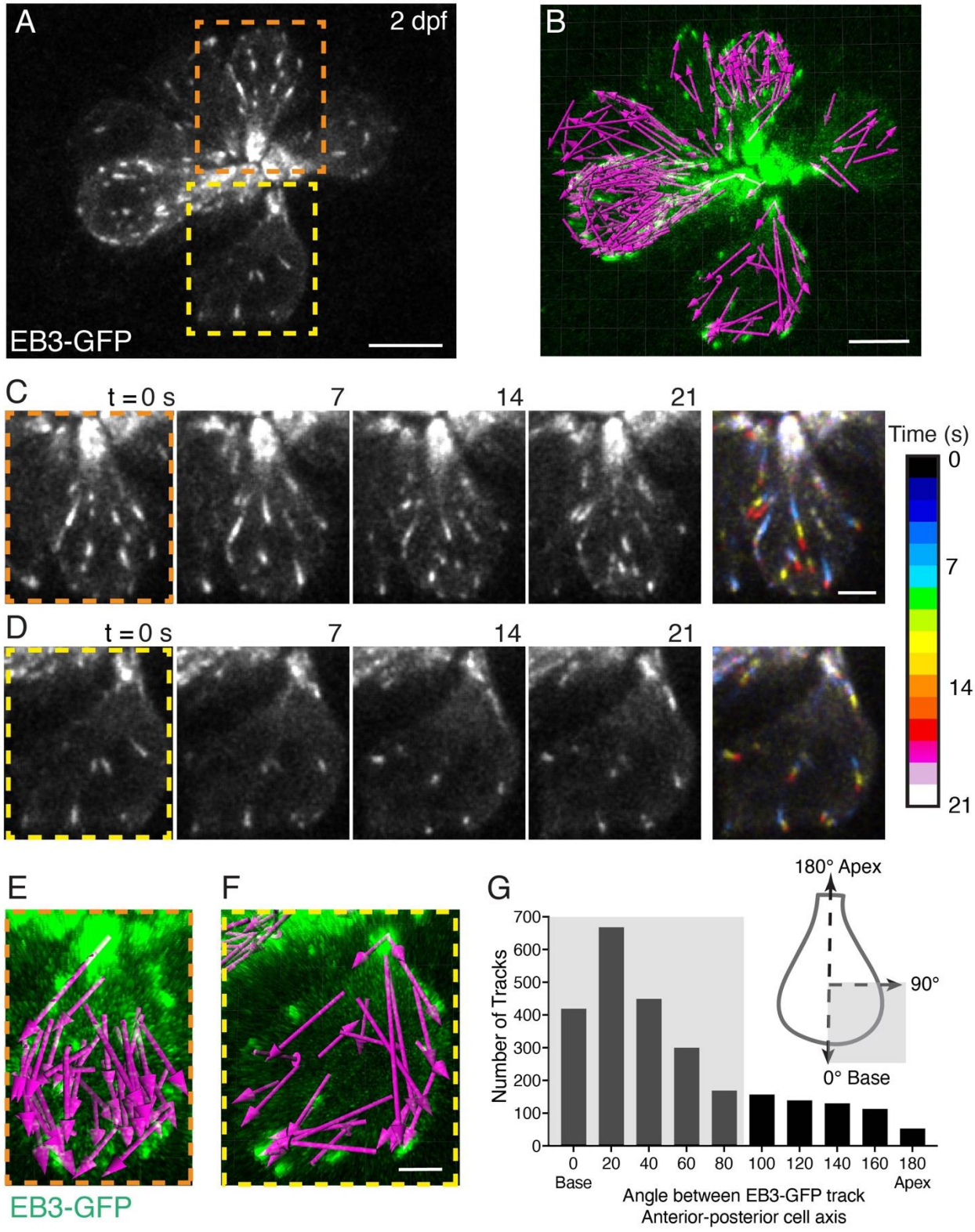

Figure 2 – EB3-GFP tracks show plus-ends of microtubules move to the cell base

1215 **A)** Example image of a neuromast at 2 dpf. The growing or plus-ends of microtubules are
1216 marked with EB3-GFP. In this example the apex of 8 developing cells is at the center of the
1217 image and the base of each cell is at the periphery. 2 example cells are outlined (dashed lines)
1218 and expanded in more detail in in **C-D,** and **E-F**. **B)** A 22 min timelapse was taken of the example
1219 in **A**. All EB3-tracks, indicated by magenta arrows (Tracked in Imaris) acquired during the
1220 timelapse are shown. **C-D)** Example time courses of EB3-GFP in hair cells over 21 s; the cell apex
1221 is towards the top of each image. In the final image, the 4 images for each example (0-21 s)
1222 were projected overtime as a pseudocolor image represented by the colormap. The
1223 pseudocolor images show that many EB3-GFP tracks move to the cell base. **E-F)** The magenta
1224 arrows in **E** and **F** show all the EB3-GFP tracks acquired in the example cells in **C-D** over the
1225 entire 22 min duration. Arrowheads indicate direction of travel. **G)** The schematic in **G** shows
1226 how EB3-GFP tracks were aligned to each hair cell. Tracks moving toward the apex have a track
1227 angle of 180°, while those moving to the base have an angle of 0°. This analysis revealed that
1228 the majority of EB3-GFP tracks (shaded domains) move toward the base of the cell (n = 7
1229 neuromasts, 2597 tracks). Scale bars in **A** = 5 µm and in **C-F** = 2 µm.
1230

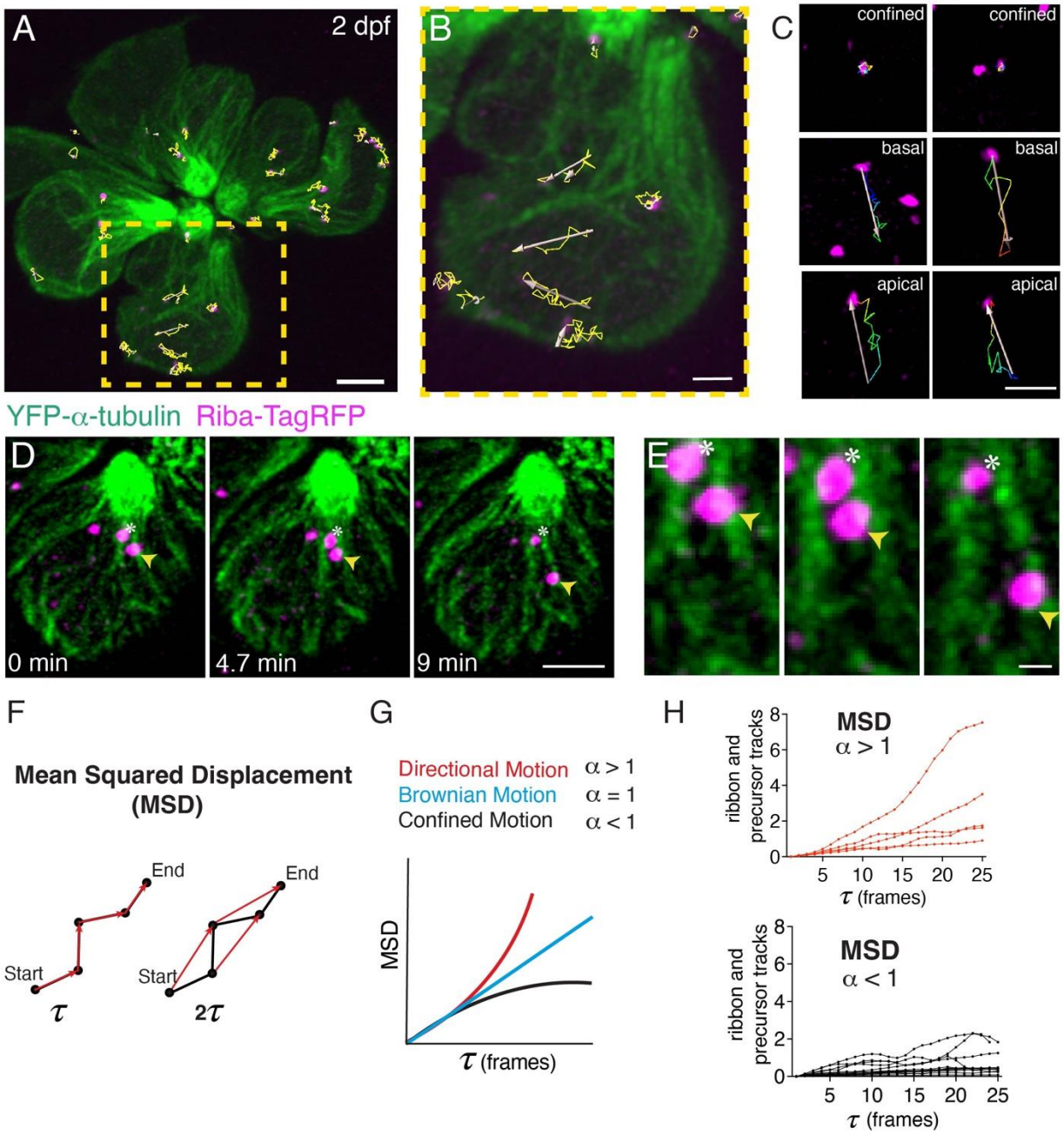

Figure 3 – Ribbon precursors exhibit directional motion and confinement on microtubules

A-B) To quantify motion, ribbons and ribbon precursors were tracked in early and intermediate stage hair cells at 2 dpf (example). Shown are tracks (in yellow) from an entire neuromast (**A**) and a single hair cell (**B**), obtained using in Imaris, during a 30 min timelapse acquired every 50 s (also see Movie S2). **C)** Magnified view showing individual tracks overtime show examples of confinement, and motion towards the cell base and apex. **D)** Example of confined motion and

1238 directed motion on microtubules in a single hair cell. Movie was obtained during a 9 min
1239 timelapse acquired every 20 s. The ribbon labeled by the asterisks remains confined, while the
1240 ribbon labeled with the yellow arrow moves along a microtubule, towards the cell base, over
1241 time. **E)** A magnified image of the example shown in **D. F)** Mean squared displacement (MSD) vs
1242 time was used to measure movement behaviors. The results are plotted in the form of MSD vs
1243 time step (τ) plots and the exponent (α) of the plots can be used to distinguish between the
1244 different types of motion observed (confined, directional or Brownian motion). Tracks that
1245 move directionally with a velocity have $\alpha > 1$, where α is the exponent of the MSD vs time
1246 curve. MSD can also reveal tracks exhibiting confined diffusion ($\alpha < 1$), i.e., bound to the
1247 microtubule but not moving. **H)** Example MSD plots of individual ribbon tracks from 2 control
1248 neuromasts (15 tracks MSD <1, 5 tracks MSD>1). The tracks that move directionally with a
1249 velocity have $\alpha > 1$ are in red, while tracks that are confined with a velocity $\alpha < 1$ are in black.
1250 Scale bar in **A** = 2 µm, **B-D** = 1 µm and in **E** = 500 nm.
1251

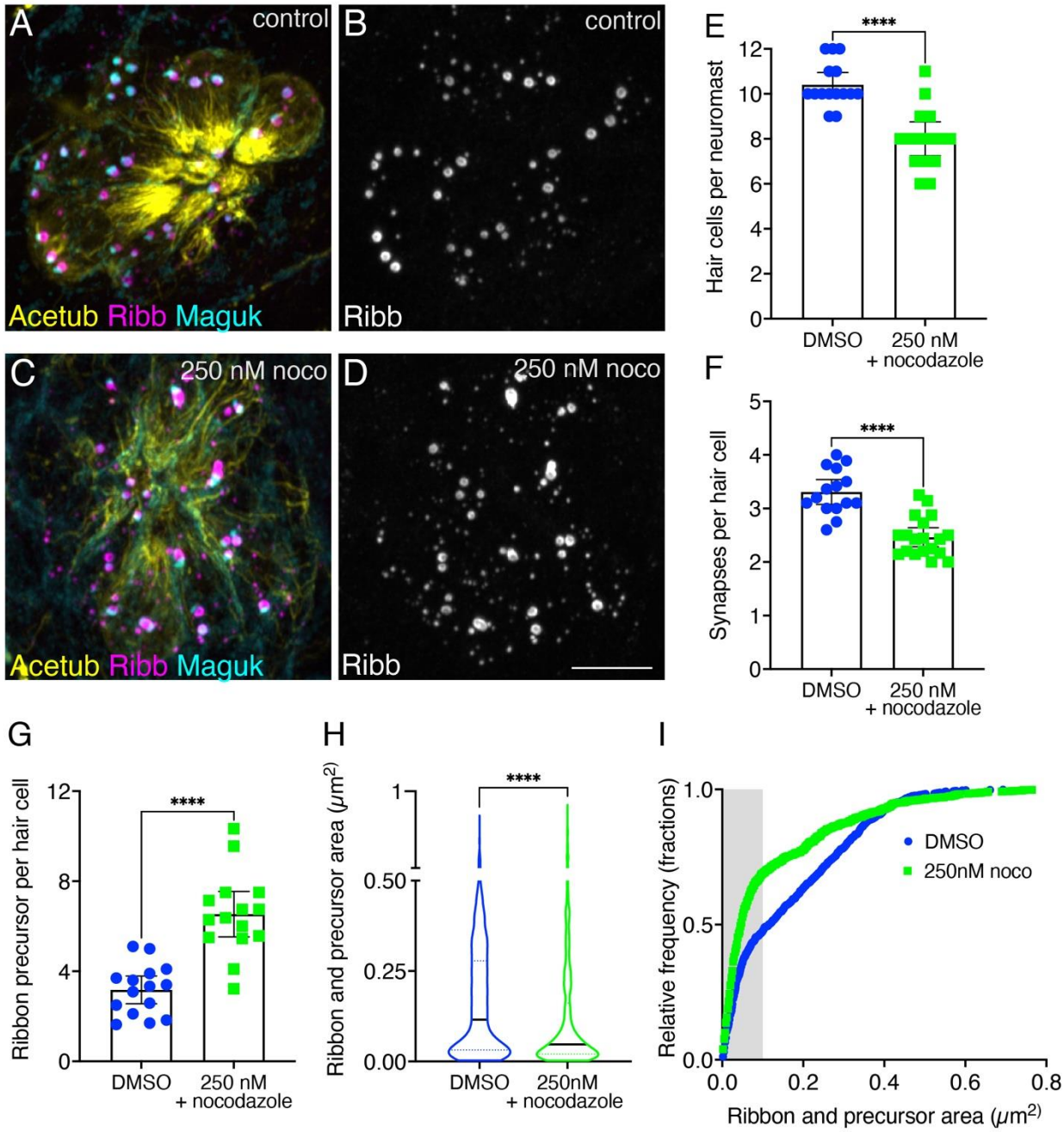

Figure 4 – Overnight microtubule destabilization increases precursor numbers and decreases synapse counts

A-D) Example immunostain of a neuromasts at 3 dpf after an overnight treatment with 250 nM nocodazole (**C-D**) or DMSO (**A-B**). Acetylated α-tubulin (Acetub) labels microtubules, Ribeyeb (Ribb) labels precursors and ribbons, and Maguk labels postsynapses. **E-G**) After an overnight treatment with 250 nM nocodazole there are significantly fewer hair cells per neuromast (**E**, P <

1259 0.0001), fewer complete synapses per cell (**F**, $P < 0.0001$), and more ribbon precursors per cell
1260 (**G**, $P < 0.0001$) compared to controls (n = 15 neuromasts for control and 250 nM nocodazole
1261 treatments). **H-I**) After an overnight treatment with 250 nM nocodazole the average area of
1262 Ribeyeb puncta was significantly lower compared to controls (**H**, $P < 0.0001$, n = 1008 and 1135
1263 Ribeyeb puncta for control and 250 nM nocodazole treatments). In **I**, the relative frequency of
1264 all the areas of Ribeyeb puncta are plotted in nocodazole treatment and controls. The shaded
1265 area in **I** shows the areas (areas < 0.1 μm^2) used to quantify precursor numbers in **G**. For
1266 comparisons an unpaired t-test was used in **E-G**, and a Mann-Whitney test was used in **H**. Scale
1267 bar in **D** = 5 µm.
1268
1269
1270
1271

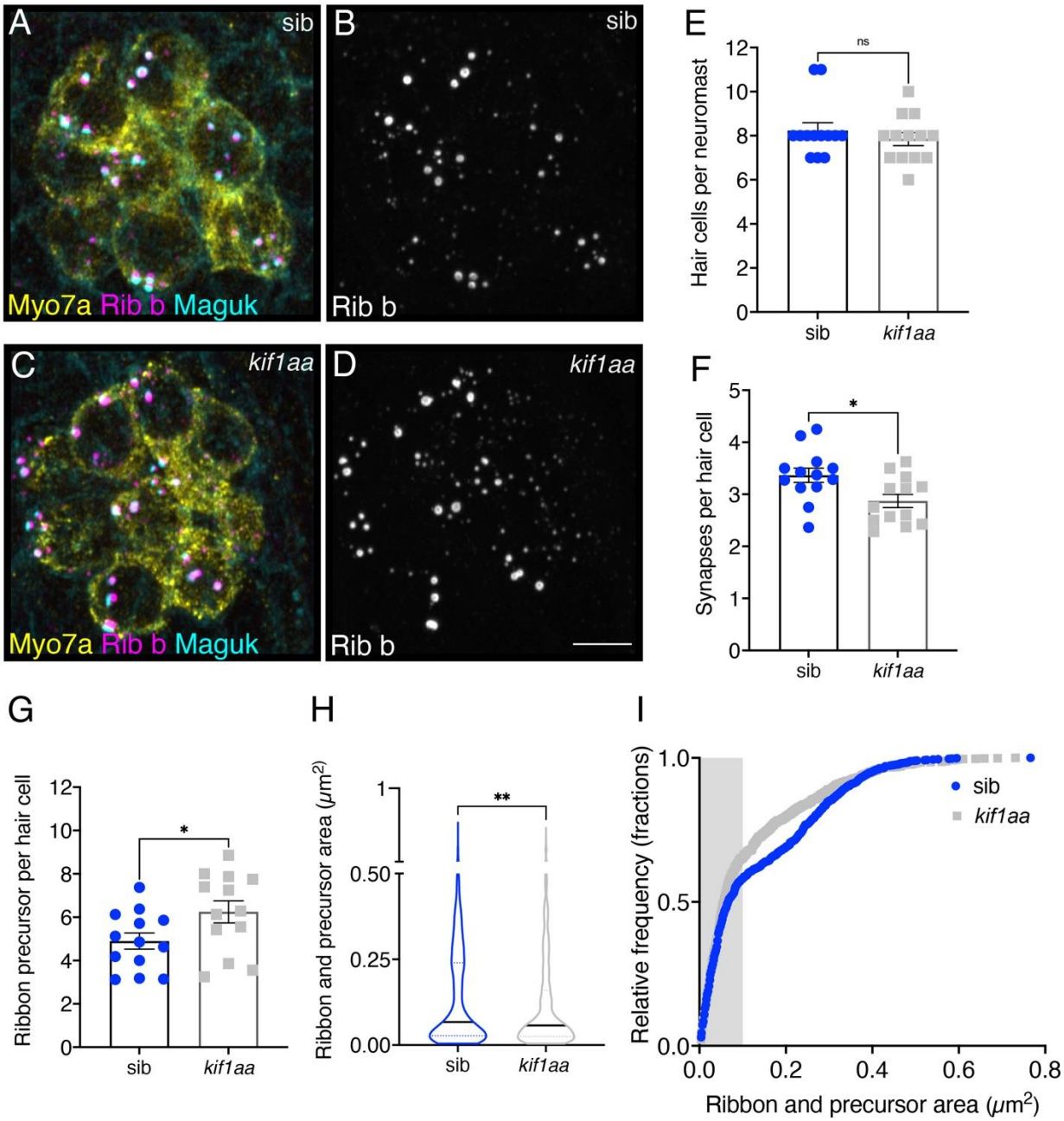

Figure 5 – Loss of Kif1aa increases precursor numbers and decreases synapse counts

A-D) Example immunostain of neuromasts at 3 dpf after in *kif1aa* germline mutants (**C-D**) or sibling control (**A-B**). Myosin7a labels hair cells, Ribeyeb (Ribb) labels precursors and ribbons, and Maguk labels postsynapses. **E-G**) In *kif1aa* mutants there is no change in the number of hair cells per neuromast (**E**, P = 0.418), but there are fewer complete synapses per cell (**F**, P = 0.014), and more ribbon precursors per cell (**G**, P = 0.044) compared to sibling controls (n = 13 neuromasts for control and *kif1aa* mutants). **H-I**) In *kif1aa* germline mutants the average area

1280 of Ribeyeb puncta was significantly lower compared to sibling controls (**H**, P = 0.005, n = 896
1281 and 1008 Ribeyeb puncta for control and *kif1aa* mutants). In **I**, the relative frequency of all the
1282 areas of Ribeyeb puncta are plotted in *kif1aa* mutants and sibling controls. The shaded area in **I**
1283 shows the areas (areas < 0.1 μm^2) used to quantify precursor numbers in **G**. For comparisons an
1284 unpaired t-test was used in **E-G**, and a Mann-Whitney test was used in **H**. Scale bar in **D** = 5 µm.
1285
1286
1287
1288
1289
1290
1291
1292
1293

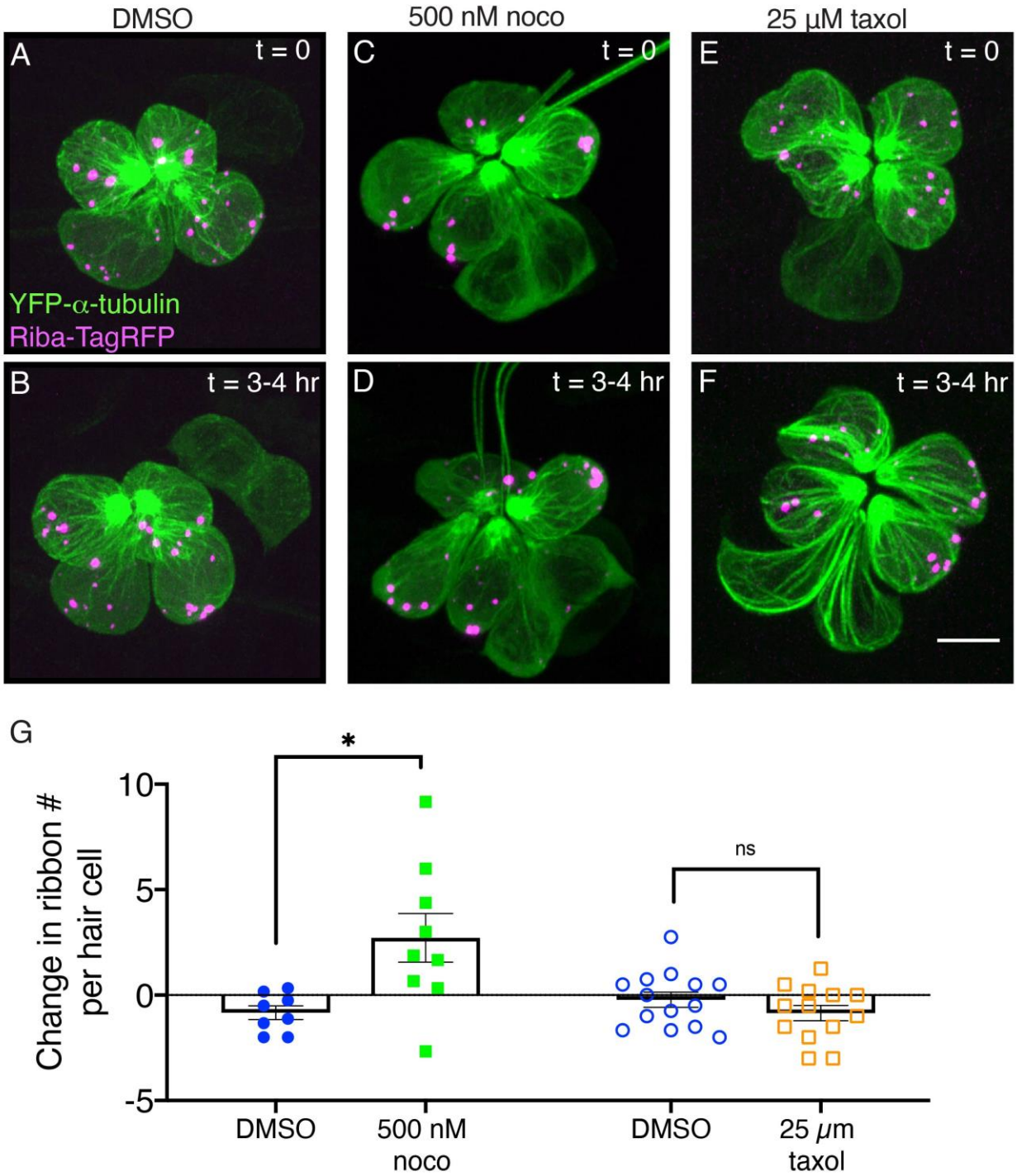

1294

1295 **Figure 6 – Microtubule destabilization increases ribbon numbers *in vivo***

1296 **A,C,E)** Example images of neuromasts at 2 dpf. The microtubule network and ribbons are

1297 marked with YFP-tubulin and Riba-TagRFP respectively. Neuromasts were imaged immediately

1298 after a 30-min treatment with DMSO (**A**, Control) 500 nM nocodazole (**C**) or 25 µM taxol (**E**), (t =

1299 0). **B,D,F**) The same neuromasts in **A,C,E** imaged 3-4 hrs after treatment. **G**) Quantification
1300 revealed that after 3-4 hr nocodazole treatment, there were more Riba-TagRFP puncta per hair
1301 cell compared to controls (n = 9 and 8 neuromasts for nocodazole and DMSO, p = 0.013). In
1302 contrast after a 3-4 hr taxol treatment there was no significant change in the number of Riba-
1303 TagRFP puncta per hair cell compared to controls (n = 13 and 14 neuromasts for taxol and
1304 DMSO, p = 0.256). An unpaired t-test was used for comparisons in **G**. Scale bar in **F** = 5 µm.
1305
1306
1307
1308
1309
1310
1311
1312
1313
1314

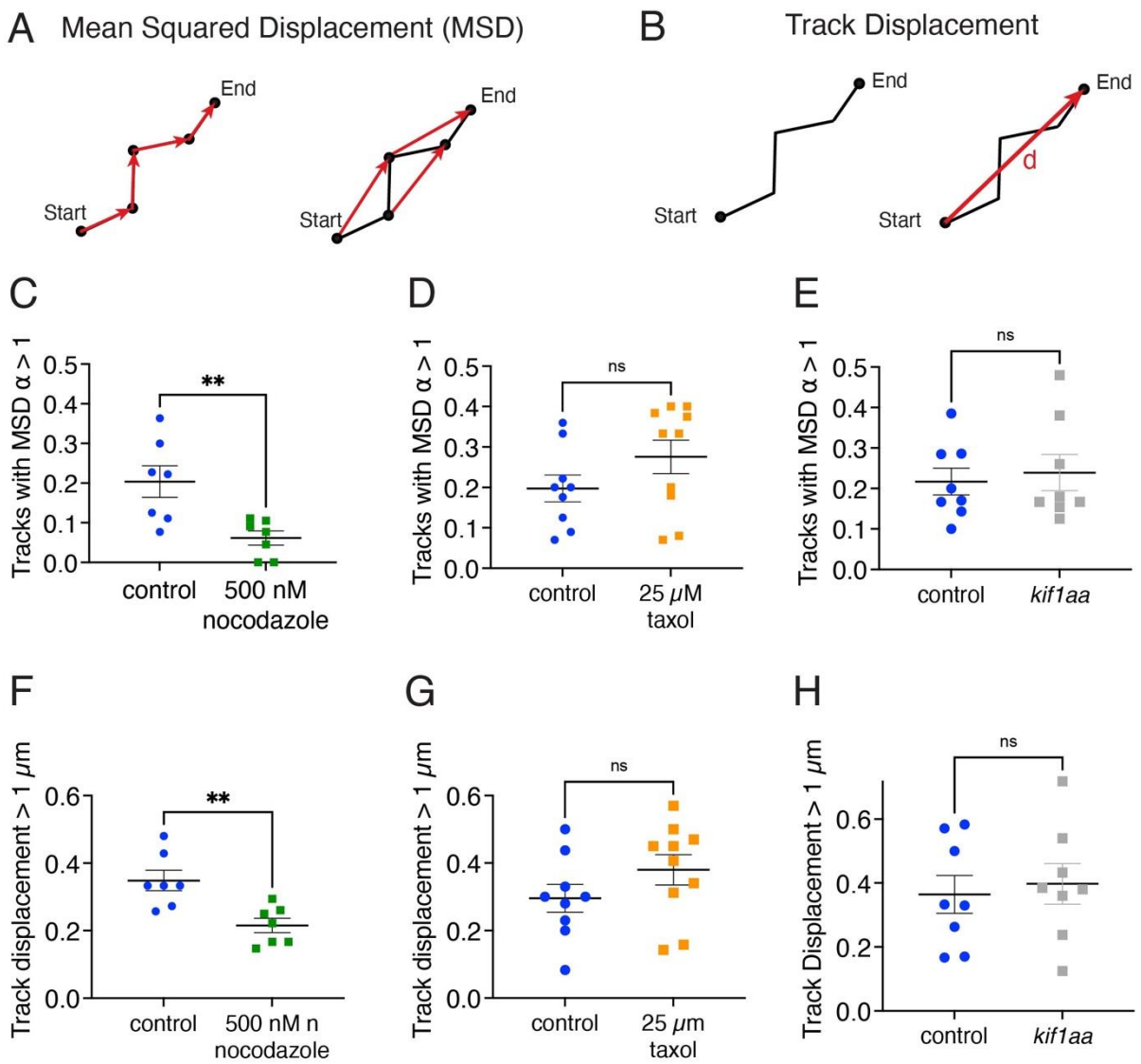

Figure 7 – Ribbon precursors require intact microtubules, but not Kif1aa for directional motion

A) Mean squared displacement (MSD) vs time was used to quantify the proportion of ribbon and precursor tracks with a velocity have $\alpha > 1$, a behavior indicative of directionally moving tracks. **B)** To further quantify directional motion, the proportion of tracks with large displacements (>1 µm) was quantified. Track displacement was measured as the distance between the start and end point of the track. **C)** Hair cells treated with 500 mM nocodazole have fewer directional tracks ($\alpha > 1$) as compared to controls ($p = 0.007$). **D)** In hair cells treated with 25 µM taxol there are not significantly fewer directional tracks ($\alpha > 1$) compared to

1325 controls (p = 0.24). **E)** In hair cells lacking Kif1aa, there are not significantly fewer directional
1326 tracks (α > 1) compared to controls (p =0.70). **F)** Hairs cells treated with 500 mM nocodazole
1327 have fewer ribbons with track displacements > 1 µm as compared to control (p = 0.004). **G)**
1328 There is no change in ribbon displacement> 1 µm in hair cells treated with 25 µM taxol (p =
1329 0.17). **H)** There is no change in ribbon displacement >1 µm in hair cells lacking Kif1aa (p = 0.71).
1330 N = 7 neuromasts for DMSO control and nocodazole for **C** and **F**; n = 9 and 10 neuromasts for
1331 DMSO control and taxol for **D** and **G**; n = 8 neuromasts for control and *kif1aa* for **E** and **H**. An
1332 unpaired t-test was used in **C-H**.
1333
1334
1335
1336
1337

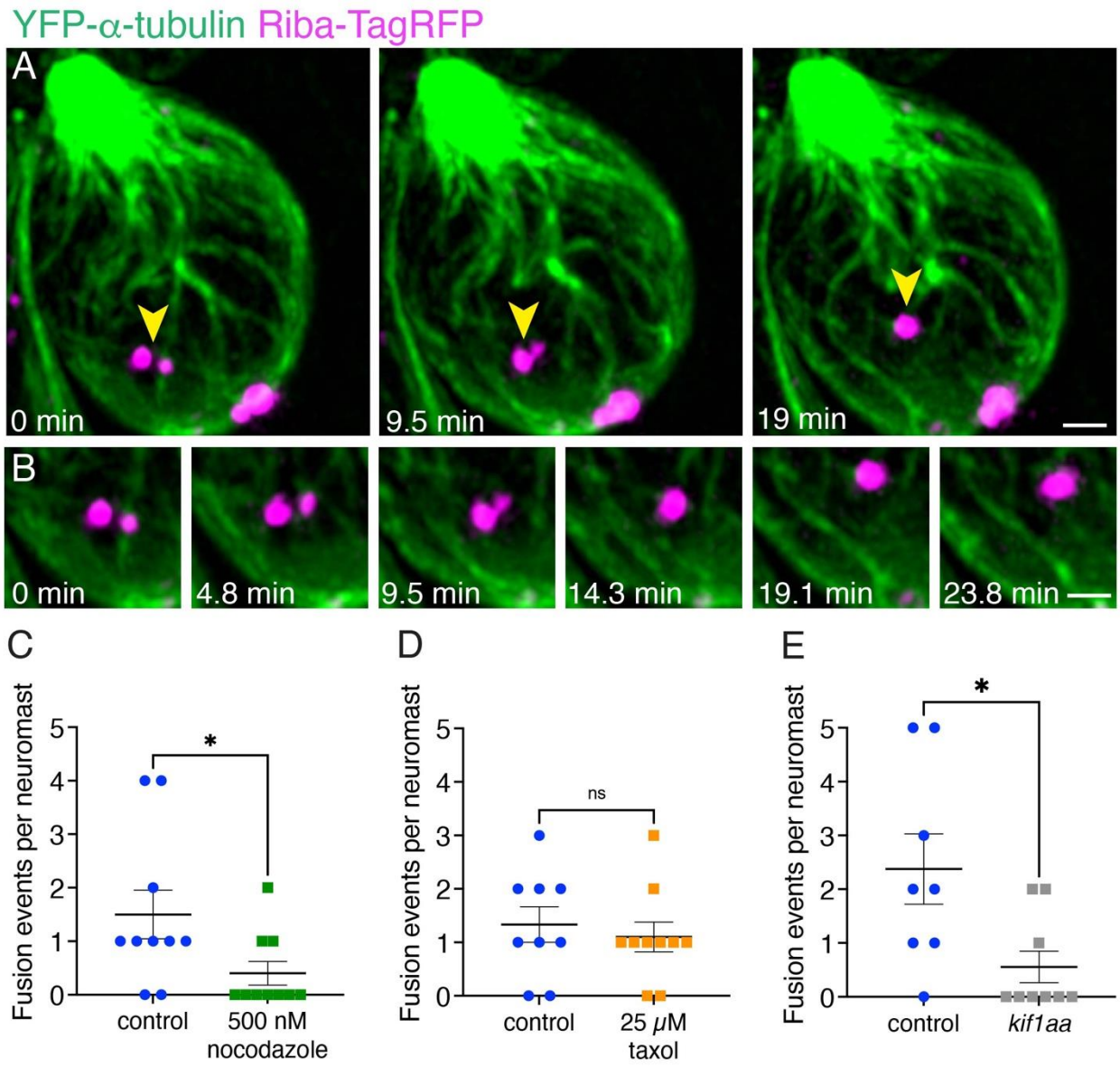

Figure 8– Ribbon precursors and Kif1aa are required for fusion events that occur on microtubules

A) An example of two ribbon precursors undergoing fusion on microtubules to form a larger ribbon (yellow arrowheads). **B)** A zoomed in montage of the example from **A** is shown where the association of each precursor with microtubules can be seen during the process of fusion (also see Movie S8). **C-D)** Destabilizing the microtubules with nocodazole treatment reduces the number of fusion events observed in timelapses ($p = 0.035$). Taxol treatment has no effect ($p = 0.60$). **E)** Loss of Kif1aa significantly reduces the number of fusion events observed in timelapses compared to control ($p = 0.018$). N = 10 neuromasts for DMSO control and nocodazole for **C**; n =

9 and 10 neuromasts for DMSO control and taxol for **D**; n = 8 and 9 neuromasts for control and *kif1aa* for **E**. An unpaired t-test was used for comparisons in **D** and **E**, and a Mann-Whitney t-test was used in **C**. Scale bars in **A** and **B** = 1 µm.

1377 **Supplemental Figures**

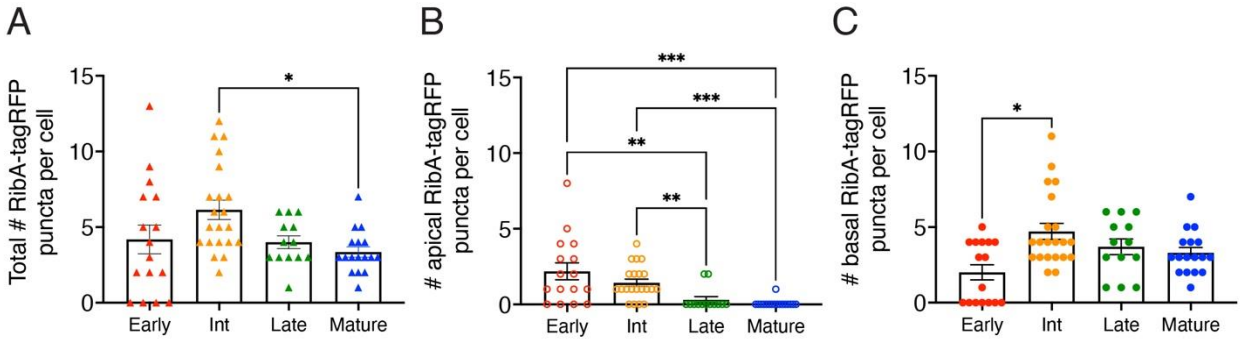

1378

1379 **Figure 1-S1 – Ribbon number and apical-basal localization changes during lateral line**

1380 **development**

1381 **A)** The total number of Riba-TagRFP puncta increases from early to intermediate stages. The

1382 total number of puncta becomes significantly reduced upon maturation. **B)** The number of

1383 apically-localized Riba-TagRFP precursors is high at early and intermediate stages, and is

1384 significantly reduced compared to late and mature hair cells. **C)** The number of basally-localized

1385 Riba-TagRFP ribbons are low at early stages, and becomes significantly higher by intermediate

1386 stages. For comparisons, a Kruskal-Wallis test was used in **A-C**.

1387

1388

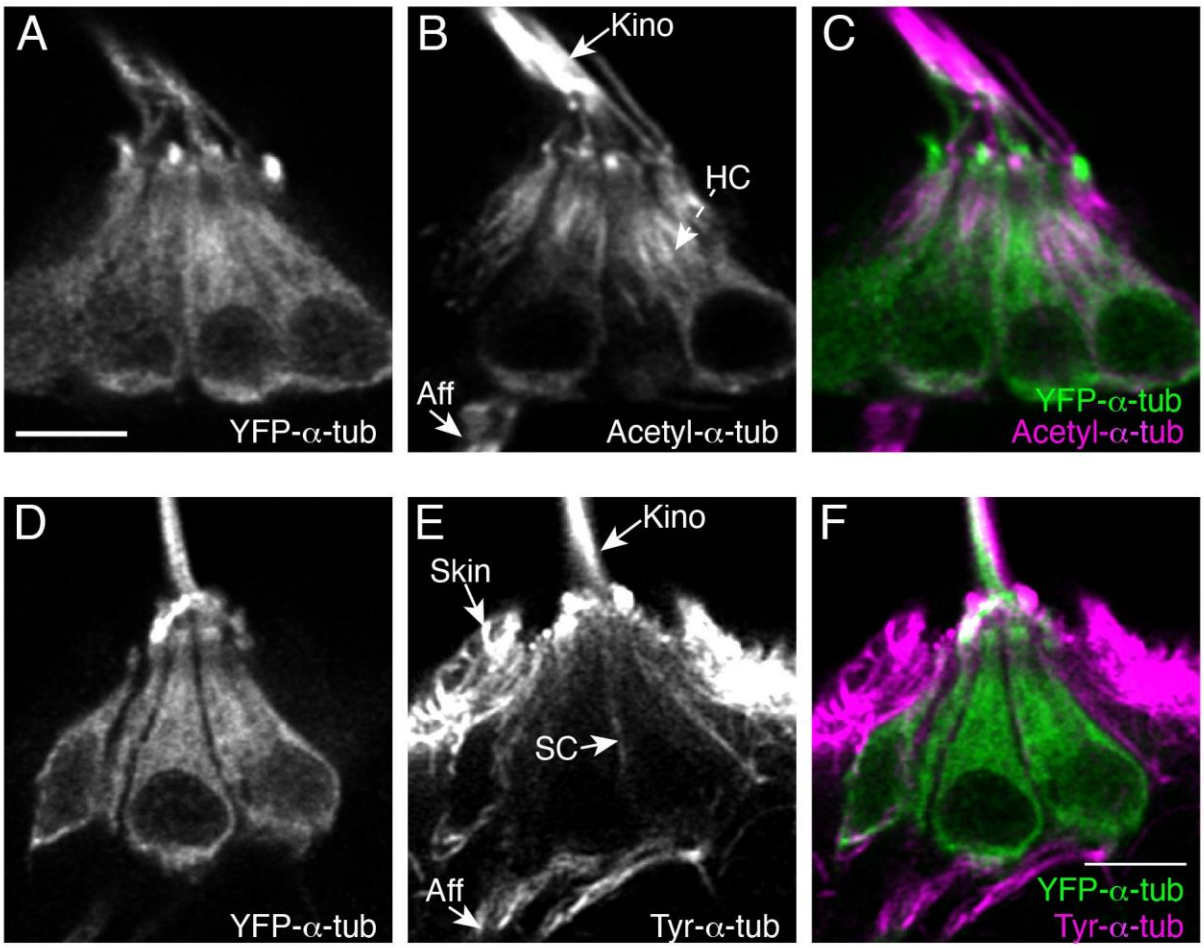

Figure 2-S1 – Microtubule modifications in lateral-line hair cells

A-F) Example immunostains of a lateral-line hair cells expressing YFP-α-tubulin at 5 dpf, labeled either with acetylated-α-tubulin (**A-C**) or tyrosinated-α-tubulin (**D-F**). Panels **A** and **D** show YFP-α-tubulin, **B** and **E** show acetylated-α-tubulin or tyrosinated-α-tubulin label respectively. Panels **C** and **F** show the merged images. HC = hair cell; SC = supporting cell; Aff = afferent process; Kino = kinocilium; Scale bar in **F** = 5 µm.

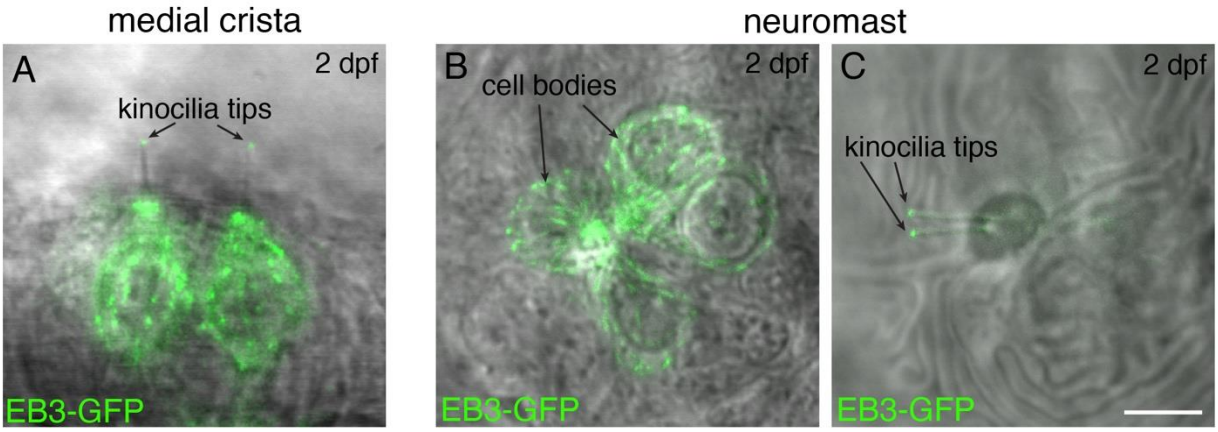

Figure 2-S2 – EB3-GFP label reveals microtubule (+) ends at kinocilial tips in lateral-line hair cells

A) Example image of EB3-GFP localization in 2 hair cells of the medial cristae within the zebrafish inner ear at 2 dpf. **B-C)** Example images of EB3-GFP localization in 4 hair cells within a lateral line neuromast at 2 dpf. In **B**, a z-projection of EB3-GFP localization in the cell bodies is shown. In **C**, a more apical projection shows the localization of EB3-GFP in the kinocilia of the same hair cells as **B**. In both zebrafish inner ear and lateral-line hair cells EB3-GFP is present in the cell bodies and at the tips of kinocilia. Scale bar in **C** = 5 µm.

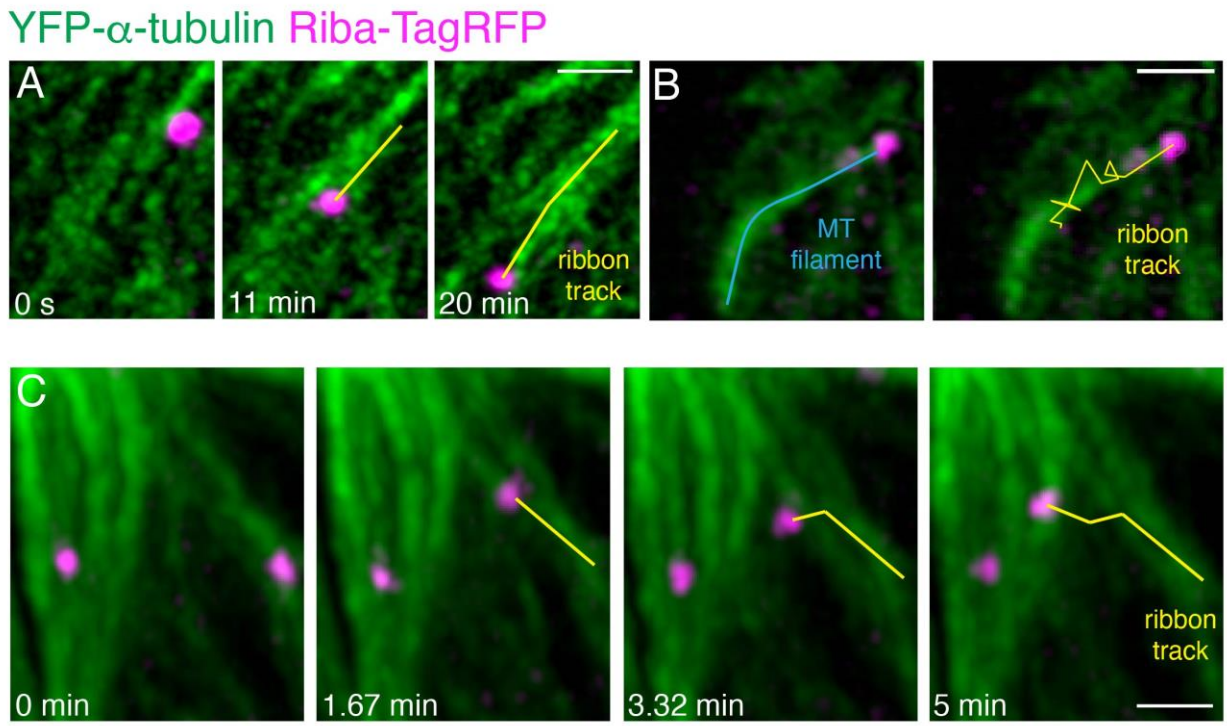

Figure 3-S1 – Ribbons move directionally on microtubules and can move between microtubule filaments

A) Example of ribbon movement on a microtubule directed towards the cells base. Ribbon precursor movement was imaged at 20 s intervals for ~40 min. Shown in **A** are frames 3, 36 and 63 (1, 12, and 21 min). **B)** Example of a ribbon movement along a microtubule towards the cell apex. Images were acquired at 50 s intervals for ~40 min. Microtubule is indicated in blue. The track of the ribbon over frames 25-46 (21 frames, 17.5 min) is shown in yellow. The track is overlaid onto the last image of the timelapse (also see Movie S5). **C)** Example of a ribbon moving along a microtubule towards the cell apex and then switching to another microtubule. Ribbon was imaged at 98 s intervals for 43 min. Shown in **C** are frames 10, 12, 14 and 16 (also see Movie S6). Scale bars in **A-C** = 1 µm.

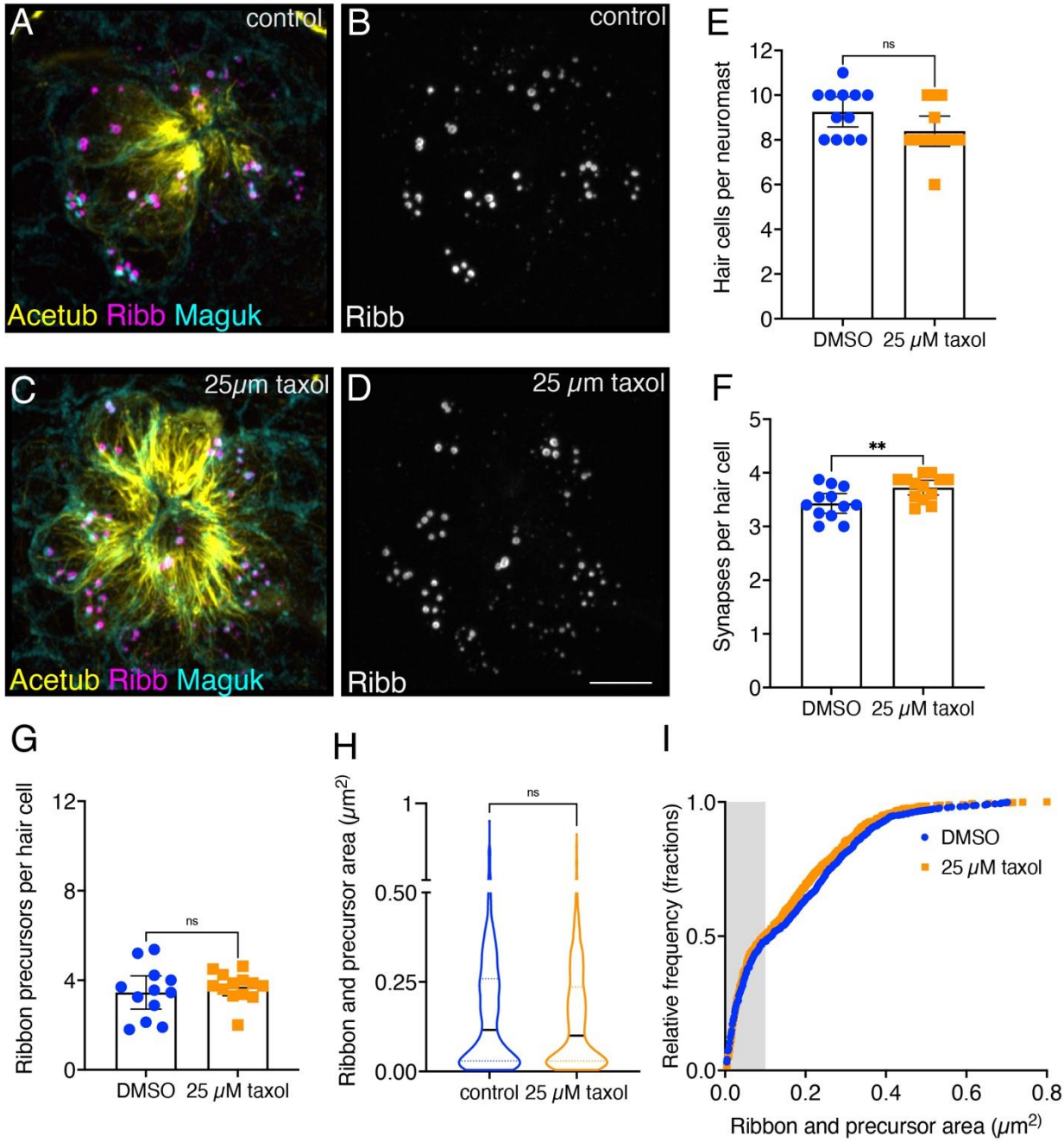

Figure 4-S1 – Overnight microtubule stabilization slightly increases synapse counts

A-D) Example immunostain of a neuromasts at 3 dpf after an overnight treatment with 25 µM taxol (**C-D**) or DMSO (**A-B**). Acetylated-α-tubulin (Acetub) labels microtubules, Ribeyeb (Ribb) labels precursors and ribbons, and Maguk labels postsynapses. **E-G**) After an overnight treatment with 25 µM taxol there are similar numbers of hair cells per neuromast (**E**, P = 0.059), more complete synapses per cell (**F**, P = 0.009), and no change in the number of ribbon

1431 precursors per cell (**G**, P = 0.398) compared to controls (n = 12 and 13 neuromasts for control
1432 and 25 µM taxol treatments). **H-I**) After an overnight treatment with 25 µM taxol the average
1433 area of Ribb puncta was not changed compared to controls (**H**, P = 0.153, n = 800 and 817 Ribb
1434 puncta for control and 25 µM taxol treatments). In **I**, the relative frequency of all the areas of
1435 Ribb puncta are plotted in taxol treatment and controls. The shaded area in **G** shows the areas
1436 (areas < 0.1 μm^2) used to quantify precursor numbers in **G**. For comparisons an unpaired t-test
1437 was used in **E-G**, and a Mann-Whitney test was used in **H**. Scale bar in **D** = 5 µm.
1438
1439
1440
1441
1442
1443
1444
1445
1446
1447

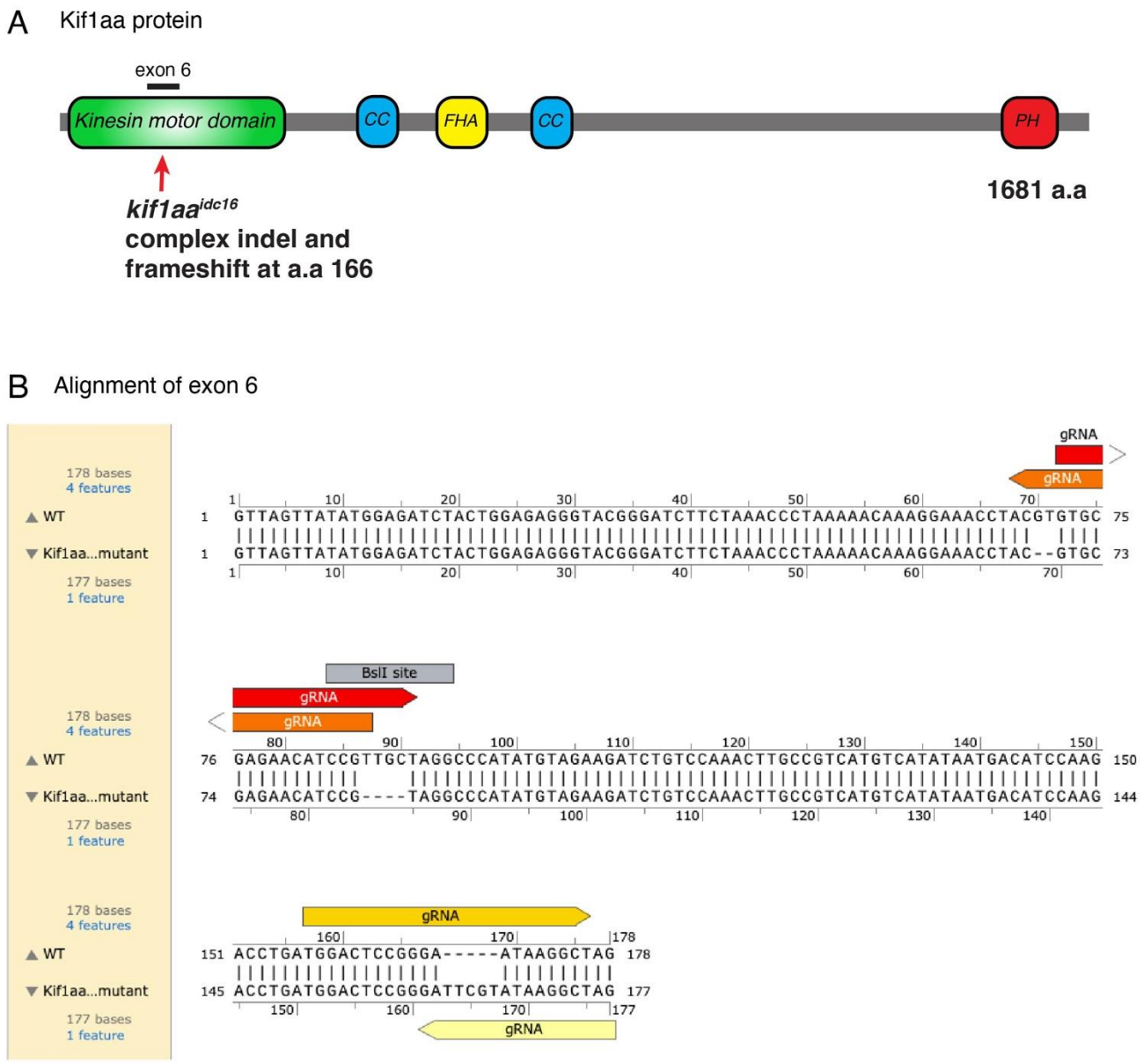

Figure 5-S1 –Kif1aa protein and exon 6 lesions

A) Overview of the Kif1aa protein and major domains (coiled coil (CC), fork-head associated (FHA), pleckstrin homology (PH)). The location of the germline *kif1aa* lesion in the Kinesin motor domain within exon 6 is indicated. **B)** The DNA sequence of exon 6 (178 bp) in wild type and *kif1aa* germline mutants. The 4 gRNAs used to make the *kif1aa* mutant are shown. 2 deletions and 1 insertion are present in *kif1aa* mutants. The BslI restriction site used for genotyping is shown. This DNA alignment was done in Snapgene.

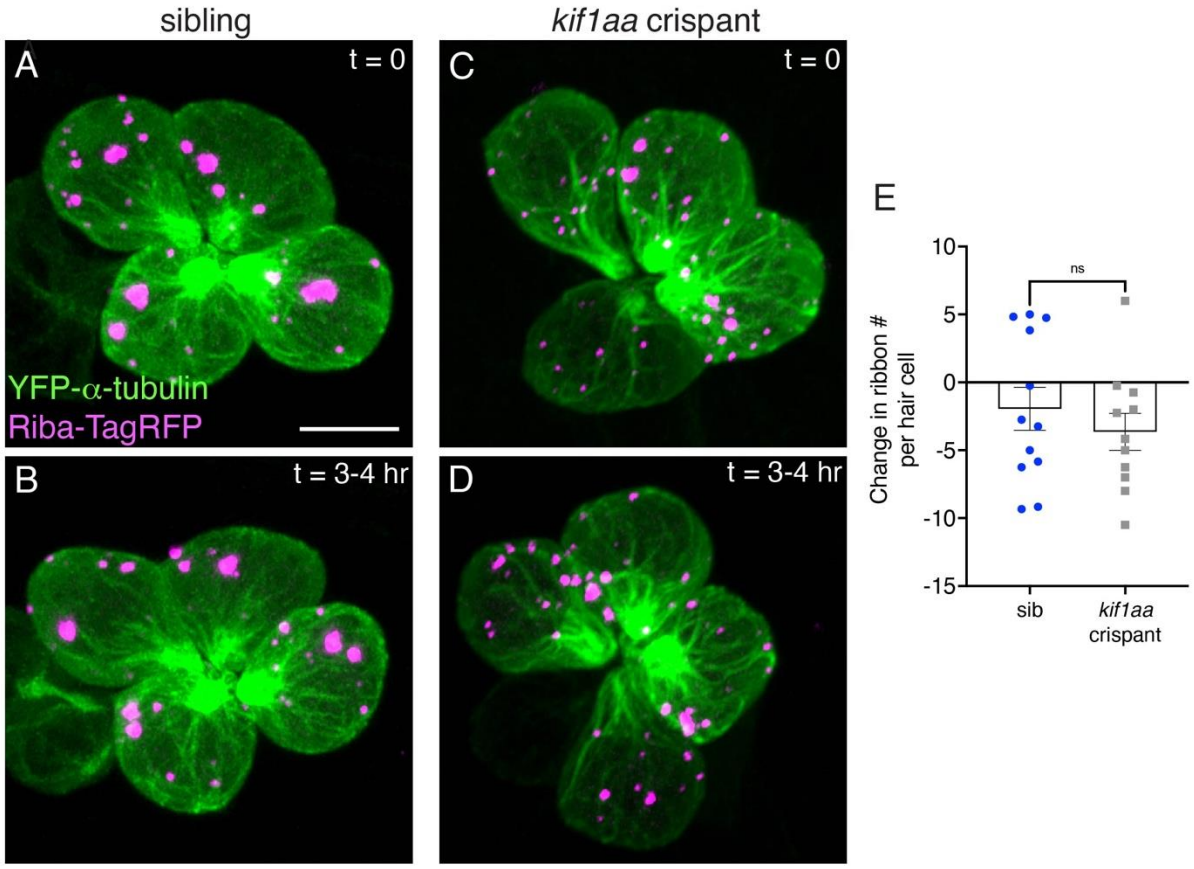

Figure 6-S1 – Loss of Kif1aa does not impact ribbon numbers over 3-4 hrs

A,C) Example images of neuromasts at 2 dpf. The microtubule network and ribbons are marked with YFP-tubulin and Riba-TagRFP respectively. Neuromasts were imaged immediately (**A**, Control; **C**, *kif1aa* F0 crispants) and after 3-4 hrs (**B**, Control; **D**, *kif1aa* F0 crispants). **E**) Quantification revealed that after 3-4 hrs the number of Riba-TagRFP puncta per hair cell was the same in control and *kif1aa* F0 crispants (n = 12 and 11 neuromasts for control and *kif1aa* F0 crispants p = 0.427). An unpaired t-test was used for comparisons in **E**. Scale bar in **A** = 5 µm.

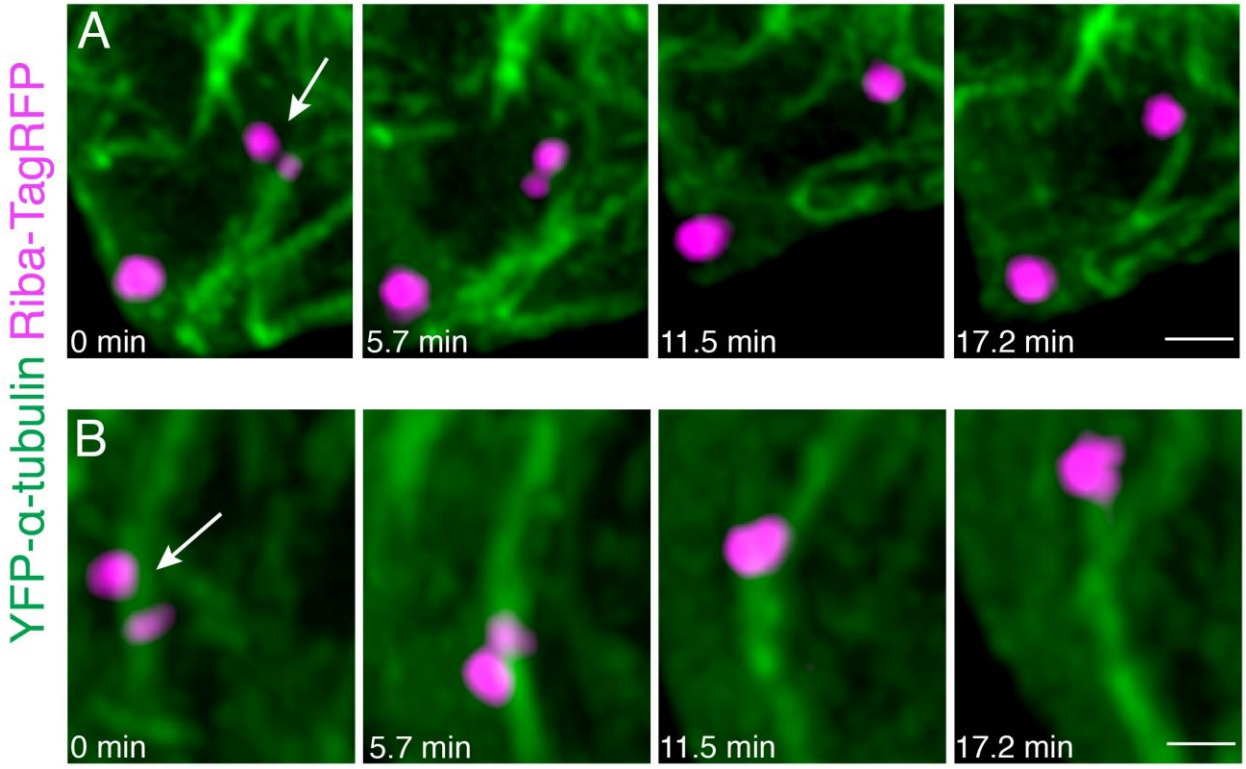

Figure 8-S1 – Ribbon precursor fuse on or near microtubules

A-B) Two examples of ribbon precursor fusion on or near microtubules. Ribbons was tracked over 13 frames that were acquired every 5.7 min. Shown in **A** are frames 3-6. Shown in **B** are frames 4-7. Arrow indicated ribbons of interest. These examples correspond to Movies S9 and S10. Scale bars in **A-B** = 1 µm.

1481 **Movie Legends**

1482 **Movie S1 – EB3-GFP dynamics in developing lateral-line hair cells**

1483 Timelapse of the example neuromast expressing EB3-GFP from Figure 2. The growing or plus-
1484 ends of microtubules can be visualized by capturing EB3-GFP dynamics. The timelapse was
1485 acquired on a LSM 780 confocal microscope every 7 s for 22 min. Maximum intensity projection
1486 of the original z-stack is shown on the left side, played at 5 frames per second. The right side
1487 shows the same movie as the left side except EB3-GFP tracks are color-coded and followed
1488 overtime using the FIJI plugin Trackmate2. Scale bar = 5 µm

1489

1490 **Movie S2 – Tracking precursors and ribbons in 3D using Imaris**

1491 Timelapse movie of a lateral-line neuromast at 2 dpf. A partial cell volume was captured at 50 s
1492 intervals for ~30 minutes with a Zeiss LSM 780 with Airyscan. Microtubules are marked with
1493 YFP-tubulin (green), ribbons and precursors are marked with Riba-TagRFP (magenta). Tracks
1494 captured in Imaris are color coded with time. This example is the same as Figure 3A-B.
1495 Maximum intensity projections of the original z-stack is shown, played at 5 frames per second.
1496 Scale bar = 2 µm.

1497

1498 **Movie S3 – Tracking precursors and ribbons in 3D using Imaris**

1499 Timelapse movie of a lateral-line neuromast at 2 dpf. A partial cell volume was captured at 60 s
1500 intervals for ~30 minutes with a Zeiss LSM 780 with Airyscan. Microtubules are marked with
1501 YFP-tubulin (green), ribbons and precursors are marked with Riba-TagRFP (magenta). Tracks
1502 captured in Imaris are shown in yellow. Maximum intensity projections of the original z-stack is
1503 shown, played at 5 frames per second. Scale bar = 2 µm.

1504

1505 **Movie S4 – Directional motion to cell base and stationary precursors on microtubule**

1506 Timelapse movie of a lateral-line neuromast at 2 dpf. A partial cell volume was captured at 20 s
1507 intervals for 9 minutes with a Zeiss LSM 980 with Airyscan 2. Microtubules are marked with
1508 YFP-tubulin (green), ribbons and precursors are marked with Riba-TagRFP (magenta). Maximum
1509 intensity projections of the original z-stack is shown, played at 5 frames per second. This

1510 example is the same as Figure 3D-E. On the left side is a timelapse of the hair cell showing a
1511 ribbon precursor moving along a microtubule towards the hair-cell base. In addition, a
1512 stationary ribbon precursor is also shown. On the right is a higher magnification view of these
1513 two ribbon precursors. The circles indicate spots identified using Trackmate, along with the
1514 track of the moving ribbon shown in yellow. Scale bar = 2 µm.
1515
1516 **Movie S5 – Directional motion of precursor along microtubule to cell apex**
1517 Timelapse movie of a lateral-line neuromast at 2 dpf. A partial cell volume was captured at 50 s
1518 intervals for 18 min with a Zeiss LSM 780 with Airyscan. Microtubules are marked with YFP-
1519 tubulin (green), ribbons and precursors are marked with Riba-TagRFP (magenta). Maximum
1520 intensity projections of the original z-stack is shown, played at 5 frames per second. On the left
1521 side is a timelapse of the hair cell showing a ribbon precursor moving along a microtubule
1522 towards the hair-cell apex. On the right is a higher magnification view of this precursor, with
1523 the tracks of the ribbon precursor during the timelapse. The circle indicate a spot identified
1524 using Trackmate, along with the track of the moving ribbon shown in yellow. This example is
1525 the same as Figure 3-S1B. Scale bar = 2 µm.
1526
1527 **Movie S6 – Precursor switching between microtubules**
1528 Timelapse movie of a lateral-line neuromast at 2 dpf. A partial cell volume was captured at
1529 ~100 s intervals for 40 minutes with a Zeiss LSM 970 with Airyscan. Microtubules are marked
1530 with YFP-tubulin (green), ribbons and precursors are marked with Riba-TagRFP (magenta).
1531 Maximum intensity projections of the original z-stack is shown, played at 5 frames per second.
1532 On the left side is a timelapse of the hair cell showing a ribbon precursor moving along a
1533 microtubule towards the hair cell apex; the precursor then moves to another microtubule. On
1534 the right is a higher magnification view of the ribbon precursor during the timelapse. The
1535 precursor movement is quite fast and at this interval can be observed twice in a single z-stack
1536 during movement between microtubules at timepoints 2,4, and 15. This example is the same as
1537 Figure 3-S1C. Scale bar = 2 µm.
1538

1539 **Movie S7 – Microtubule dynamics in hair cells change upon treatment with nocodazole and**
1540 **taxol**
1541 Timelapse movies of lateral-line neuromasts at 2 dpf captured after treatment with 0.1 %
1542 DMSO (Control, left side), 25 µM taxol (Taxol, middle) or 250 nM nocodazole (Noc, right side)
1543 for 30 minutes. Microtubules are marked with YFP-tubulin (gray) and ribbons are marked with
1544 Riba-TagRFP (magenta). The timelapses were acquired in 3 um z-stacks (Zeiss LSM 780 with
1545 Airyscan) every 60 s for 30 min. Maximum intensity projections of the original z-stacks are
1546 shown here, played at 5 frames per second. The taxol-treated neuromast has less dynamic
1547 microtubules and very little cytoplasmic tubulin (depolymerized tubulin), indicating that the
1548 microtubules are more stable than the control. In the nocodazole-treated neuromast, there are
1549 less microtubules and more diffuse cytoplasmic tubulin compared to the control. Scale bar = 2
1550 µm.
1551
1552 **Movie S8 – Ribbon precursors attached to microtubules undergo fusion to form larger ribbons**
1553 Timelapse movie of a lateral-line neuromast at 2 dpf. A partial cell volume of 3 µm was
1554 captured at 4.8 min intervals for 100 minutes with a Zeiss LSM 780 with Airyscan. Microtubules
1555 are marked with YFP-tubulin (green) and ribbons are marked with Riba-TagRFP (magenta).
1556 Maximum intensity projections of the original z-stacks are shown, played at 5 frames per
1557 second. This example is the same as Figure 8D-E. Two ribbon precursors associate with
1558 microtubules and fuse near the hair cell base. Scale bar = 2 µm.
1559
1560 **Movie S9 – Ribbon precursors attached to microtubules undergo fusion to form larger ribbons**
1561 Timelapse movie of a lateral-line neuromast at 2 dpf. A partial cell volume of 3 µm was
1562 captured at 5.7 min intervals for 75 minutes with a Zeiss LSM 780 with Airyscan. Microtubules
1563 are marked with YFP-tubulin (green) and ribbons are marked with Riba-TagRFP (magenta).
1564 Maximum intensity projections of the original z-stacks are shown, played at 2 frames per
1565 second. Scale bar = 2 µm.
1566

1567 **Movie 10 – Ribbon precursors attached to microtubules undergo fusion to form larger**
1568 **ribbons**
1569 Timelapse movie of a lateral-line neuromast at 2 dpf. A partial cell volume of 3 µm was
1570 captured at 5.7 min intervals for 75 minutes with a Zeiss LSM 780 with Airyscan. Microtubules
1571 are marked with YFP-tubulin (green) and ribbons are marked with Riba-TagRFP (magenta).
1572 Maximum intensity projections of the original z-stacks are shown, played at 2 frames per
1573 second. Scale bar = 2 µm.
1574
1575
1576
1577
1578